Two-dimensional bifurcation phenomena in thermal convection in horizontal, concentric annuli containing saturated porous media

By K. HIMASEKHAR and HAIM H. BAU†

Department of Mechanical Engineering and Applied Mechanics, University of Pennsylvania, Philadelphia, PA 19104–6315, USA

A saturated porous medium confined between two horizontal cylinders is considered. As a result of a temperature difference between the cylinders, thermal convection is induced in the medium. The flow structure is investigated in a parameter space (R, Ra) where R is the radii ratio and Ra is the Darcy–Rayleigh number. In particular, the cases of $R = 2$, $2^{\frac{1}{2}}$, $2^{\frac{1}{4}}$ and $2^{\frac{1}{8}}$ are considered. The fluid motion is described by the two-dimensional Darcy–Oberbeck–Boussinesq's (DOB) equations, which we solve using regular perturbation expansion. Terms up to $O(Ra^{60})$ are calculated to obtain a series presentation for the Nusselt number Nu in the form

$$Nu(Ra^2) = \sum_{s=0}^{30} N_s Ra^{2s}.$$

This series has a limited range of utility due to singularities of the function $Nu(Ra^2)$. The singularities lie both on and off the real axis in the complex Ra^2 plane. For $R = 2$, the nearest singularity lies off the real axis, has no physical significance, and unnecessarily limits the range of utility of the aforementioned series. For $R = 2^{\frac{1}{2}}$, $2^{\frac{1}{4}}$ and $2^{\frac{1}{8}}$, the singularity nearest to the origin is real and indicates that the function $Nu(Ra^2)$ is no longer unique beyond the singular point.

Depending on the radii ratio, the loss of uniqueness may occur as a result of either (perfect) bifurcations or the appearance of isolated solutions (imperfect bifurcations). The structure of the multiple solutions is investigated by solving the DOB equations numerically. The nonlinear partial differential equations are converted into a truncated set of ordinary differential equations via projection. The steady-state problem is solved using Newton's technique. At each step the determinant of the Jacobian is evaluated. Bifurcation points are identified with singularities of the Jacobian. Linear stability analysis is used to determine the stability of various solution branches. The results we obtained from solving the DOB equations using perturbation expansion are compared with those we obtained from solving the nonlinear partial differential equations numerically and are found to agree well.

1. Introduction

Natural convection in porous media is germane to many technologies involving thermal insulators such as steam distribution lines, gas lines in gas-cooled nuclear reactors, cryogenics and storage of thermal energy. Thermal insulators typically

---

† All correspondence should be directed to this author.

consist of a fibrous material, which is permeable to fluid motion and thus subject to natural convection. As Caltagirone (1976), Burns & Tien (1979), Brailovskaya, Petrazhitskii & Polezhaev (1978), and others have demonstrated, this natural convection may contribute significantly to the heat transfer process.

In this paper, we focus on the two-dimensional convective motion in a horizontal, concentric annulus containing a saturated porous medium. It turns out that two-dimensional flows are physically realizable for low Darcy–Rayleigh numbers, small radii-ratio annuli, and annuli with small axial lengths.

A similar configuration has been studied both experimentally and theoretically by Caltagirone (1976). He carried out experiments involving an annulus of radii ratio $R = 2$. His theoretical work covers the parameter range $2^{\frac{1}{4}} \leqslant R \leqslant 16$. Caltagirone (1976) has observed that for relatively low Rayleigh numbers Ra, the flow is two-dimensional and steady, consisting of two counter-rotating cells, one in each half of the annulus. As the Rayleigh number increases beyond some critical value Ra_c, the flow undergoes a Hopf bifurcation into a three-dimensional, oscillatory motion. Caltagirone (1976) concluded that multicellular, two-dimensional structures do not exist. In a later, numerical study, Rao, Fukuda & Hasegawa (1986) demonstrated the existence of a multicellular flow structure in an annulus of radii ratio $R = 2$, which they claim (mistakenly, as we shall show later) bifurcates from the bicellular convective structure at some $Ra = Ra_c$. Thus, there seems to be some confusion over what happens as the Rayleigh number is increased. In this paper, we systematically investigate the structure of the flow in parameter space (R, Ra), $2^{\frac{1}{2}} \leqslant R \leqslant 2$.

It is hoped that this study also will contribute to our understanding of thermal convection of Newtonian fluids in a concentric annulus.

We employ two different theoretical tools. The first one consists of constructuring an approximate solution to the governing equations using a power series expansion in terms of the Rayleigh number Ra. Terms up to $O(Ra^{60})$ are computed. The radius of convergence of the series is limited owing to singularities located in the complex Ra plane.

The singularities lie on and off the real axis. The singularities off the real axis have no physical significance. The singularities which lie on the real axis and are denoted Ra_1 correspond to the region $Ra < Ra_1$, in which the function $Nu(Ra^2)$ is unique and the solution of the Darcy–Oberbeck–Boussinesq (DOB) equations is also likely to be unique. For $Ra > Ra_1$, multiple solutions exist.

The mechanism through which the solution loses uniqueness is investigated by solving the nonlinear partial differential equations (p.d.e.'s) directly. To this end, we employ Galerkin's technique to convert the p.d.e.'s into ordinary differential equations (o.d.e.'s). The steady-state problem consists of a truncated set of nonlinear algebraic equations.

A solution branch for the algebraic system is generated by starting from a known solution (i.e. the conduction solution) and continuing the solution for higher values of the Rayleigh number using Newton's technique. The procedure is successful as long as the system's Jacobian is not singular. Bifurcation points correspond to the values of the Rayleigh number for which the Jacobian becomes singular. It turns out that for radii ratios R of less than $2^{\frac{1}{2}}$, the appearance of multiple solutions occurs as a result of a (perfect) bifurcation, while for $R \geqslant 2^{\frac{1}{2}}$ the appearance of multiple solutions occurs as a result of the existence of additional isolated solutions (i.e. imperfect bifurcation). The results obtained from the power series expansion and the numerical solution of the nonlinear p.d.e.'s are compared and found to agree well.

Two-dimensional bifurcation phenomena, of course, are not the only type that
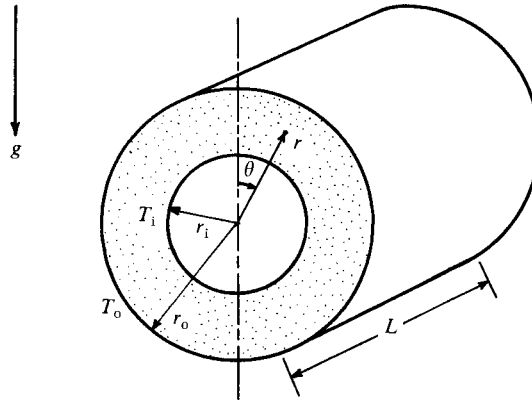
FIGURE 1. The geometric configuration.

occur in thermal convection in horizontal annuli. For example, Caltagirone (1976) observed transition from two-dimensional flow into three-dimensional oscillatory flow. Thus, in order to determine the range of validity of the two-dimensional model, it is important to establish whether two- or three-dimensional bifurcations are the first to occur. We do so by comparing our own results with Caltagirone's (1976) and conclude that for small radii ratios and for narrow annuli, two-dimensional bifurcations are likely to precede the three-dimensional ones. Thus, the results of this study are applicable only to small radii ratios and/or narrow gaps.

2. Mathematical model

A concentric, horizontal annulus of axial length L is filled with a saturated porous medium (figure 1). The inner and outer cylinders of radii r_i and r_o are maintained at constant uniform temperatures $\hat{T}_i$ and $\hat{T}_o$, respectively. As a result of the temperature difference, $\Delta\hat{T} = \hat{T}_i - \hat{T}_o$, buoyancy-driven flow is induced in the medium. In this paper, we focus on two-dimensional flows. Such flows are likely to exist for either small temperature differences $\Delta\hat{T}$, small aspect ratios $A = L/r_i$ or small radii ratios $R = r_o/r_i$. The fluid motion is governed by the two-dimensional Darcy–Oberbeck–Boussinesq (DOB) equations which are expressed below in dimensionless form using a cylindrical coordinate system (r, θ):

$$\left.\begin{aligned} \nabla^2\psi &= Ra\left(\sin\theta\,\frac{\partial T}{\partial r} + \frac{1}{r}\cos\theta\,\frac{\partial T}{\partial \theta}\right), \\ \frac{\partial T}{\partial t} &= \nabla^2 T - \frac{1}{r}\frac{\partial(\psi, T)}{\partial(\theta, r)}, \end{aligned}\right\} \qquad (2.1)$$

with the boundary conditions

$$\psi = 0, \quad T = 1 \quad \text{at } r = 1, \qquad 0 \leqslant \theta \leqslant \pi,$$

$$\psi = T = 0 \qquad \text{at } r = R, \qquad 0 \leqslant \theta \leqslant \pi,$$

$$\frac{\partial T}{\partial \theta} = \psi = 0 \qquad \text{at } 1 \leqslant r \leqslant R, \quad \theta = o, \pi.$$

As the boundary conditions indicate, we restrict ourselves to symmetric solutions with respect to the vertical axis ($\theta = 0, \pi$).

Usually in this paper we shall concern ourselves with the steady-state version of (2.1) in which the time-dependent term is absent. Nevertheless, we write the DOB equations (2.1) in the more general transient form in order to facilitate the linear stability analysis described in §4.3. In this context, the steady-state solutions will serve as initial data for the time-dependent equations. In the above equations, ψ represents the stream function and T is the temperature. $Ra = \kappa\beta g r_i \Delta T/\nu\alpha_{eq}$ is the Darcy–Rayleigh number; where β is the thermal expansion coefficient; κ is the medium's permeability; g is the gravitational acceleration; ν is the kinematic viscosity of the saturating fluid; α_{eq} is the equivalent thermal diffusivity of the medium; and t is time. All quantities are non-dimensional. The lengthscale is the radius of the inner cylinder r_i, the temperature scale is $\Delta\hat{T}$, the velocity scale is α_{eq}/r_i and the timescale is $\sigma r_i^2/\alpha_f$. α_f is the fluid's thermal diffusivity; σ is the ratio between the thermal capacity of the fluid and the equivalent thermal capacity of the saturated medium.

For the subsequent derivation, we find it convenient to map the annular domain ($r_i \leqslant r \leqslant r_o$, $0 \leqslant \theta \leqslant \pi$) onto the rectangle ($0 \leqslant x \leqslant \log R$, $0 \leqslant y \leqslant \pi$). To the end, we employ the conformal transformation $x + iy = \log r + i\theta$. The resulting equations are

$$\nabla^2\psi = Ra \, e^x \left[\sin y \frac{\partial T}{\partial x} + \cos y \frac{\partial T}{\partial y} \right], \qquad (2.2a)$$

$$e^{2x} \frac{\partial T}{\partial t} = \nabla^2 T - \frac{\partial(\psi, T)}{\partial(y, x)}, \qquad (2.2b)$$

with the boundary conditions

$$\psi = 0, \quad T = 1 \quad \text{at } x = 0, \qquad 0 \leqslant y \leqslant \pi,$$

$$\psi = T = 0 \qquad \text{at } x = \log R, \qquad 0 \leqslant y \leqslant \pi,$$

and

$$\psi = \frac{\partial T}{\partial y} = 0 \qquad \text{at } 0 \leqslant x \leqslant \log R, \quad y = 0, \pi.$$

The heat flow rate is presented in terms of the Nusselt number,

$$Nu = -\frac{\log R}{\pi} \int_0^\pi \left(\frac{\partial T}{\partial x}\right)\bigg|_{x = 0 \text{ or } \log R} dy, \qquad (2.3)$$

which corresponds to the ratio of the total heat transfer to the heat transfer in the absence of convection.

We proceed by seeking steady-state solutions for (2.2) and then analysing the stability of these solutions. The steady-state equations are obtained by omitting the time derivatives from (2.2).

3. An extended perturbation expansion

The governing equations (2.2) are a set of coupled nonlinear, partial differential equations for which an exact solution is not known. In this section, we construct an approximate, steady-state solution using a regular perturbation expansion.

3.1. *The expansion*

We consider the dependent variables (ψ, T) to be functions of both the coordinates (x, y) and the Rayleigh number Ra. The expansion of ψ and T into truncated Taylor series in terms of Ra yields:

$$\psi(Ra; x, y) \sim \sum_{s=1}^{S} Ra^s \psi_s(x, y), \tag{3.1a}$$

$$T(Ra; x, y) \sim \sum_{s=0}^{S} Ra^s T_s(x, y), \tag{3.1b}$$

and

$$Nu(Ra^2) \sim \sum_{s=0}^{\frac{1}{2}S} Ra^{2s} N_s. \tag{3.1c}$$

The dependence of the Nusselt number on Ra^2 rather than on Ra itself follows from the expected invariance of the Nusselt number to a change of sign of Ra. This conjecture is, of course, verified later on by the analysis.

By introducing the above expansions into the nonlinear p.d.e.'s (2.2) and by equating coefficients of like powers in Ra, we obtain a set of linear p.d.e.'s:

$$\nabla^2 T_s = \epsilon_s \sum_{k=1}^{s-1} \frac{\partial(\psi_k, T_{s-k})}{\partial(y, x)}, \tag{3.2a}$$

$$\nabla^2 \psi_s = \epsilon_s \, e^x \left(\sin y \frac{\partial T_{s-1}}{\partial x} + \cos y \frac{\partial T_{s-1}}{\partial y} \right), \tag{3.2b}$$

where

$$\epsilon_s = \begin{cases} 0 \text{ for } s = 0 \\ 1 \text{ otherwise,} \end{cases}$$

and the boundary conditions are

$$T_s = (1 - \epsilon_s), \quad \psi_s = 0 \quad \text{at } x = 0, \qquad 0 \leqslant y \leqslant \pi,$$

$$T_s = \psi_s = 0 \qquad \text{at } x = \log R, \qquad 0 \leqslant y \leqslant \pi,$$

and

$$\frac{\partial T_s}{\partial y} = \psi_s = 0 \qquad \text{at } 0 \leqslant x \leqslant \log R, \quad y = 0, \pi.$$

The zeroth-order solution corresponds to the no-motion state:

$$\psi_0 = 0, \quad T_0 = 1 - \frac{x}{\log R}, \quad N_0 = 1. \tag{3.3}$$

In principle, one could solve (3.2) analytically to any desired order. For example, Caltagirone (1976) calculated terms up to $O(Ra^2)$ and $O(Ra^3)$, respectively, in the temperature and stream-function expansions. However, the amount of labour and the length of the expressions involved tend to increase exponentially as the order of approximation s increases. At the present time, it appears that the analytical evaluation of higher-order terms may not be feasible even if computer algebra (i.e. MACSYMA) were to be employed. Thus, we resort to a numerical approach and use a Galerkin method to integrate the Poisson equations (3.2). The dependent variables (ψ_s, T_s) are expressed using the truncated spectral presentations:

$$\left. \begin{array}{l} \psi_s(x, y) \sim \sum_{n=1}^{N} \sum_{m=1}^{M} A_{s,m,n} \sin\left(\frac{m\, c_{11}\, x}{\log R}\right) \sin(ny), \\ T_s(x, y) \sim \sum_{n=0}^{N} \sum_{m=1}^{M} B_{s,m,n} \sin\left(\frac{m\pi x}{\log R}\right) \cos(ny), \end{array} \right\} \quad s \geqslant 1. \tag{3.4}$$

By requiring (3.4) to satisfy (3.2) in the sense of weighted residuals, we obtain recurrence relationships for the coefficients $A_{s,m,n}$ and $B_{s,m,n}$. The corresponding expressions are given in Appendix A.

Caltagirone's (1976) work suggests a certain symmetry in this problem, which is reflected in the coefficients $A_{s,m,n}$ and $B_{s,m,n}$. One can show (by induction) that each of the functions T_s and ψ_s is even (odd) in y if s is an even (odd) integer. This implies that non-zero values of $A_{s,m,n}$ and $B_{s,m,n}$ occur only when $n \leqslant s$ and s and n are either both odd or both even. The aforementioned fact was exploited in determining the coefficients $A_{s,m,n}$ and $B_{s,m,n}$ numerically, and it is consistent with the assumption that the Nusselt number is a function of Ra^2 as expressed by (3.1c).

The coefficients N_s in the Nusselt-number expansion (3.1c) can be expressed as

$$N_s = - \sum_{m=1}^{M} (m\pi) B_{2s,m,0}. \tag{3.5}$$

A double-precision Fortran program was written to evaluate the coefficients $A_{s,m,n}$ and $B_{s,m,n}$ for various choices of the radii ratio R and the truncation levels (M, N and S). The effect of the machine's finite precision on the results (round-off error) was tested by running the program with 18- and 27-digits precision. The results in each case were essentially the same. Similarly, the impact of the level of truncation was examined by running the program for a number of choices of M and N. M and N were assumed to be sufficiently large when further increases in their values did not alter the first four significant digits of N_s. For a more detailed discussion of the effect of round-off error and truncation see Appendix B.

Of prime interest to our subsequent discussion is the Nusselt number Nu which can be expressed as

$$Nu \sim \sum_{s=0}^{\frac{1}{2}S} N_s Ra^{2s}. \tag{3.6}$$

The computed coefficients N_s are given in table 1 for $S = 60$ and radii ratios of $R = 2$, $2^{\frac{1}{2}}$, $2^{\frac{1}{4}}$ and $2^{\frac{1}{8}}$.

Series such as (3.6) often have a limited radius of convergence Ra_c. We attempt to estimate this radius of convergence in the next subsections. For $Ra < Ra_c$, the series (3.1) may be used to calculate the flow and temperature fields and the Nusselt number. The corresponding flow (stream-function) and temperature (isotherms) fields are depicted in Figures 11(a) and 13(a) for $R = 2^{\frac{1}{2}}$ and $2^{\frac{1}{4}}$, respectively. The flow field (left-hand sides of the figures) corresponds to bicellular convection, that is one convective cell in each half of the annulus. Warm fluid is rising next to the hot, inner cylinder and descending next to the cold, outer one. The temperature field depicted in the right-hand sides of the figures resembles the conductive regime. The isotherms are almost concentric which suggests that convective effects are relatively weak.

3.2. The range of utility of the series

We start the investigation of the radius of convergence of the series (3.5) by employing the Cauchy root and the ratio tests (Fulks 1961; Lang 1985). These two tests are quite universal and do not require any a priori assumptions about the analytic structure of the function $Nu(Ra^2)$.

R (M,N) s	2 $(32,32)$	$2^{\frac{1}{2}}$ $(31,31)$	$2^{\frac{1}{4}}$ $(31,31)$	$2^{\frac{1}{8}}$ $(32,32)$
0	$+1.0000\mathrm{E}+000$	$+1.0000\mathrm{E}+000$	$+1.0000\mathrm{E}+000$	$+1.0000\mathrm{E}+000$
1	$+1.7276\mathrm{E}-004$	$+8.3440\mathrm{E}-006$	$+4.4867\mathrm{E}-007$	$+2.5862\mathrm{E}-008$
2	$-1.6747\mathrm{E}-008$	$-5.7059\mathrm{E}-011$	$-1.8329\mathrm{E}-013$	$-6.2571\mathrm{E}-016$
3	$+7.5606\mathrm{E}-013$	$+4.7205\mathrm{E}-016$	$+1.0395\mathrm{E}-019$	$+2.1795\mathrm{E}-023$
4	$+2.9247\mathrm{E}-016$	$-3.0750\mathrm{E}-021$	$-6.3543\mathrm{E}-026$	$-8.6474\mathrm{E}-031$
5	$-1.4378\mathrm{E}-019$	$+2.8890\mathrm{E}-027$	$+3.7746\mathrm{E}-032$	$+3.6354\mathrm{E}-038$
6	$+2.0768\mathrm{E}-023$	$+6.5721\mathrm{E}-031$	$-1.8946\mathrm{E}-038$	$-1.5608\mathrm{E}-045$
7	$+4.7895\mathrm{E}-027$	$-3.6832\mathrm{E}-036$	$+5.9087\mathrm{E}-045$	$+6.7354\mathrm{E}-053$
8	$+1.9769\mathrm{E}-030$	$+8.7719\mathrm{E}-040$	$+7.0594\mathrm{E}-051$	$-3.0760\mathrm{E}-060$
9	$-1.2009\mathrm{E}-033$	$+4.6882\mathrm{E}-044$	$+2.4773\mathrm{E}-056$	$+2.2160\mathrm{E}-067$
10	$-8.7974\mathrm{E}-037$	$+3.7726\mathrm{E}-048$	$+2.0690\mathrm{E}-061$	$-4.0551\mathrm{E}-074$
11	$+3.7281\mathrm{E}-040$	$+2.8670\mathrm{E}-052$	$+2.7152\mathrm{E}-066$	$+1.4048\mathrm{E}-080$
12	$+1.2522\mathrm{E}-043$	$+2.1574\mathrm{E}-056$	$+2.8665\mathrm{E}-071$	$-5.1189\mathrm{E}-087$
13	$-7.9484\mathrm{E}-047$	$+1.6321\mathrm{E}-060$	$+4.0072\mathrm{E}-076$	$+2.7066\mathrm{E}-093$
14	$+1.0942\mathrm{E}-050$	$+1.2208\mathrm{E}-064$	$+5.6760\mathrm{E}-081$	$-1.0414\mathrm{E}-099$
15	$+5.2079\mathrm{E}-054$	$+9.1347\mathrm{E}-069$	$+8.9018\mathrm{E}-086$	$+9.9158\mathrm{E}-106$
16	$-9.7137\mathrm{E}-057$	$+6.7863\mathrm{E}-073$	$+1.4612\mathrm{E}-090$	$-1.4429\mathrm{E}-112$
17	$+3.8873\mathrm{E}-060$	$+5.0361\mathrm{E}-077$	$+2.5253\mathrm{E}-095$	$+8.1717\mathrm{E}-118$
18	$+1.4210\mathrm{E}-063$	$+3.7184\mathrm{E}-081$	$+4.5184\mathrm{E}-100$	$+5.2931\mathrm{E}-124$
19	$-1.2857\mathrm{E}-066$	$+2.7412\mathrm{E}-085$	$+8.3304\mathrm{E}-105$	$+1.6654\mathrm{E}-129$
20	$+1.6184\mathrm{E}-070$	$+2.0129\mathrm{E}-089$	$+1.5704\mathrm{E}-109$	$+2.7102\mathrm{E}-135$
21	$+6.8192\mathrm{E}-074$	$+1.4758\mathrm{E}-093$	$+3.0133\mathrm{E}-114$	$+6.6026\mathrm{E}-141$
22	$-4.5768\mathrm{E}-077$	$+1.0784\mathrm{E}-097$	$+5.8594\mathrm{E}-119$	$+1.5074\mathrm{E}-146$
23	$+3.1477\mathrm{E}-080$	$+7.8691\mathrm{E}-102$	$+1.1510\mathrm{E}-123$	$+3.9434\mathrm{E}-152$
24	$-5.9128\mathrm{E}-084$	$+5.7255\mathrm{E}-106$	$+2.2783\mathrm{E}-128$	$+1.0725\mathrm{E}-157$
25	$-3.9819\mathrm{E}-087$	$+4.1603\mathrm{E}-110$	$+4.5347\mathrm{E}-133$	$+3.1351\mathrm{E}-163$
26	$+8.9016\mathrm{E}-091$	$+3.0152\mathrm{E}-114$	$+9.0627\mathrm{E}-138$	$+9.6316\mathrm{E}-169$
27	$-5.7448\mathrm{E}-096$	$+2.1827\mathrm{E}-118$	$+1.8164\mathrm{E}-142$	$+3.1162\mathrm{E}-174$
28	$+4.9092\mathrm{E}-097$	$+1.5763\mathrm{E}-122$	$+3.6478\mathrm{E}-147$	$+1.0536\mathrm{E}-179$
29	$-1.5003\mathrm{E}-100$	$+1.1372\mathrm{E}-126$	$+7.3352\mathrm{E}-152$	$+3.7114\mathrm{E}-185$
30	$-9.0863\mathrm{E}-104$	$+8.1851\mathrm{E}-131$	$+1.4762\mathrm{E}-156$	$+1.3561\mathrm{E}-190$
Ra_c	47	120	220	472

TABLE 1. The coefficients N_s in the original series $Nu = \sum_{s=0}^{\frac{1}{2}S} N_s Ra^{2s}$. The numbers (M,N) indicate the level of truncation (3.4).

The Cauchy root test

According to the Cauchy root test, the radius of convergence Ra_c of the series can be determined from the limit process

$$Ra_c = \lim_{s \to \infty} |N_s|^{-1/2s}. \tag{3.7}$$

Hence, in figure 2, we depict $|N_s|^{-\frac{1}{2}s}$ as a function of s for radii ratios $R = 2, 2^{\frac{1}{2}}, 2^{\frac{1}{4}}$ and $2^{\frac{1}{8}}$. Clearly, as s increases, $|N_s|^{-\frac{1}{2}s}$ approaches asymptotically a finite limit. The asymptotic value, denoted by a dashed line in figure 2, was obtained using other means (to be described later). The Cauchy root test establishes that the series does indeed have a limited radius of convergence. Unfortunately, the convergence to the asymptotic value is slow. On the other hand, the test has the advantage of being relatively insensitive to oscillatory behaviour of the coefficients N_s in the series (3.6).
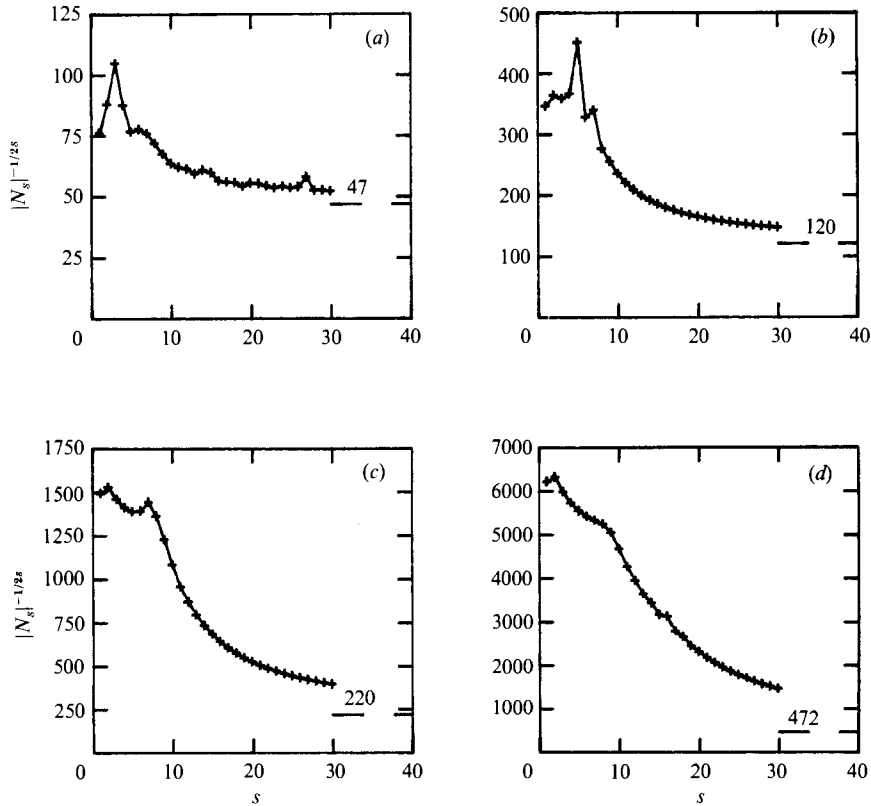
FIGURE 2. Cauchy root test. (a) $R = 2$, (b) $2^{\frac{1}{2}}$, (c) $2^{\frac{1}{4}}$ and (d) $2^{\frac{1}{8}}$.

The ratio test

In contrast to the Cauchy test, the ratio test converges quite quickly. Unfortunately, though, it is sensitive to oscillatory behaviour by the series' coefficients. To determine the radius of convergence Ra_c of the series (3.6) using this test, one can conveniently employ Domb & Sykes' (1957) simple graphical approach (see also Gaunt & Guttmann 1974). To this end, we plot in figure 3 the ratio $|N_s/N_{s-1}|$ as a function of s^{-1}. Ra_c is estimated as the limiting value

$$Ra_c^2 = \lim_{s \to \infty} \left| \frac{N_{s-1}}{N_s} \right|. \tag{3.8}$$

For the radii ratio $R = 2$, the Domb–Sykes plot is too oscillatory to yield any useful results. In this particular case, the Cauchy root test clearly has an advantage over the ratio test (compare figures 3a and 2a). In the other cases considered (i.e. $R = 2^{\frac{1}{2}}$, $2^{\frac{1}{4}}$ and $2^{\frac{1}{8}}$) the curves eventually demonstrate an almost linear relationship with s^{-1}. We extrapolate the data to $s \to \infty$ by fitting polynomials of various orders of s^{-1} into the graph of the ratio (N_s/N_{s-1}) *vs.* s^{-1}. We then use the resulting formula to estimate the value of Ra_c. This is accomplished by constructing a Neville table (Gaunt & Guttmann 1974; see also Appendix C for details). For $R = 2^{\frac{1}{2}}$ and $2^{\frac{1}{4}}$, the Neville table predicts $Ra_c = 120 \pm 3$ and 220 ± 5. For $R = 2^{\frac{1}{8}}$, linear extrapolation predicts $Ra_c = 366$ while quadratic extrapolation leads to erratic behaviour which precludes one from reaching a definitive conclusion. Apparently, in this case, we need a larger
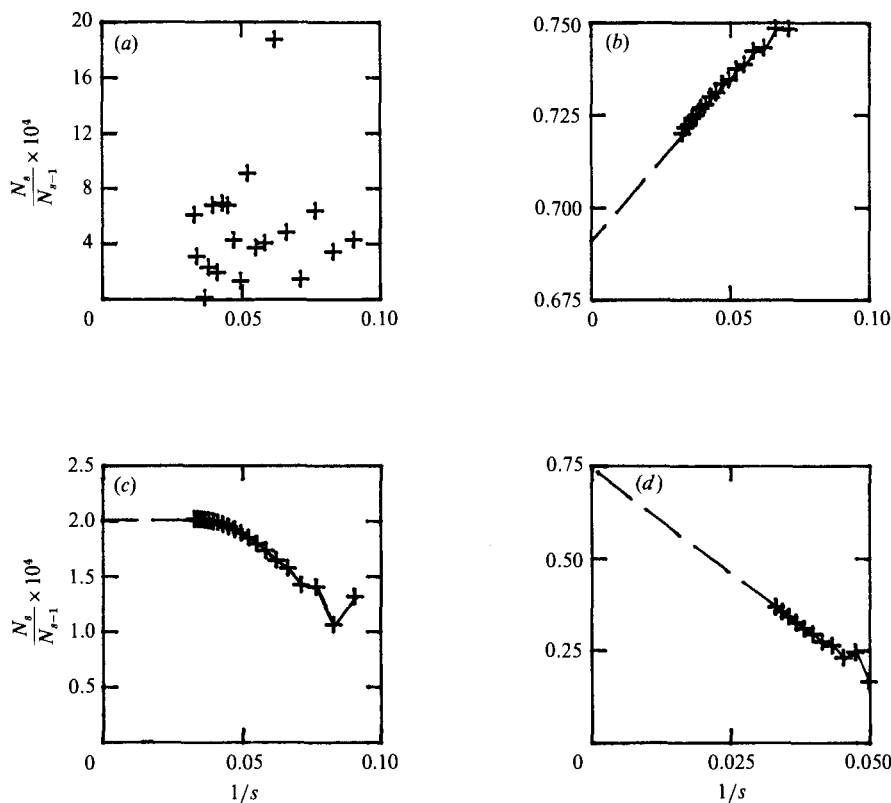
FIGURE 3. Domb–Sykes plots for the original series (3.6). (a) $R = 2$, (b) $2^{\frac{1}{2}}$, (c) $2^{\frac{1}{4}}$ and (d) $2^{\frac{1}{8}}$.

number of terms in the series (3.6) than we currently have. We did not procure these additional terms owing to budget constraints. Alternatively, we estimated Ra_c using the Padé method which we describe later (§3.3).

The Darboux Theorem

   To obtain additional estimates of the radius of convergence of the series (3.6) and the nature of the nearest singularity, it is necessary to hypothesize about the analytic structure of the function $Nu(Ra^2)$. To this end, we use the Darboux theorem (Henrici 1977; Hunter & Guerrier 1980). Briefly, the Darboux theorem states that if the singularity of the function $Nu(z)$ $(z \equiv Ra^2)$ that is closest to the origin is located at the real point $z = z_1$ and the behaviour of $Nu(z)$ in its neighbourhood is given by

$$Nu(z) = \left(1 - \frac{z}{z_1}\right)^{-\nu} r(z) + h(z) \quad \nu \neq 0, \; -1, \; -2, \; \ldots, \tag{3.9}$$

where
$$r(z) = \sum_{k=0}^{\infty} r_k (z - z_1)^k$$

and $r(z)$ and $h(z)$ are analytic in a circle with a centre at $z = 0$ and a radius $\rho > |z_1|$, then the asymptotic expansion for N_s for large s will be

$$N_s \sim \sum_{k=0}^{\infty} \frac{(-)^k r_k z_1^{k-s} \, \Gamma(s + \nu - k)}{s \, ! \, \Gamma(\nu - k)}. \tag{3.10}$$

When s is sufficiently large, the first term in the series (3.10) is predominant, so that

$$N_s \sim \frac{r_0 \, s^{\nu-1}}{z_1^s \, \Gamma(\nu)}.$$

To the first approximation, we have

$$\frac{N_s}{N_{s-1}} \sim \frac{1}{z_1}\left[1 + \frac{\nu-1}{s} + O\!\left(\frac{1}{s^2}\right)\right]. \tag{3.11}$$

This immediately suggests that all (N_s) will ultimately have the same sign if z_1 is positive. This is the case for the expansions for radii ratios $R = 2^{\frac{1}{2}}$, $2^{\frac{1}{4}}$ and $2^{\frac{1}{8}}$.

If $Nu(z)$ were of the Darboux form, (3.9), the Domb–Sykes curves (figure 3) also might provide an estimate for the power ν in (3.9). Such an estimate could be obtained by having the straight lines in figure 3 intercept the s^{-1} axis at $s^{-1} = (1-\nu)^{-1}$. Accordingly, we predict $\nu \sim 2.3$, 1 and -14.4 for $R = 2^{\frac{1}{2}}$, $2^{\frac{1}{4}}$ and $2^{\frac{1}{8}}$, respectively. Positive values of ν, however, must be rejected on physical grounds since they imply $Nu \to \infty$ as $Ra \to Ra_c$, (3.9). In fact, the results of §4 suggest that Ra_c is a branch point with $\nu < 0$. We cannot explain with certainty why (3.11) fails to predict the correct value of the exponent ν. One plausible explanation is that the existence of non-physical singularities located close to or on the perimeter of the disc of regularity leads to wrong estimates of the exponent ν (Gaunt & Guttmann 1974, p. 188). To give credence to this speculation, we study in Appendix D a simple model function through which we demonstrate that the analysis of a truncated Taylor series may lead to an erroneous prediction of the exponent ν even though it allows one to estimate the location of the nearest singular point with good precision. In all the cases studied in this paper, it appears that the complex Ra^2 plane is populated with complex singularities (§3.3 and figure 4). Some of the complex singularities are located fairly close to the disc of analyticity. Thus, it is possible that the aforementioned non-physical singularities lead to erroneous estimates of the exponent ν. Another possibility is that the function $Nu(Ra^2)$ is not of the Darboux form (3.9).

3.3. The singularities of $Nu(Ra^2)$

The limited radius of convergence of series like (3.6) is often due to the presence of a pole or a branch point located in the complex Ra^2 plane. Some indication of the location of such a singularity can be obtained by examining the sign pattern of the coefficients N_s in the series (3.6) (Van Dyke 1974, 1975). In the case of the radii ratio $R = 2$, the sign pattern (table 1) is quite complicated. This suggests that the nearest singularity is off the real axis. On the other hand, in the cases of radii ratios $R = 2^{\frac{1}{2}}$, $2^{\frac{1}{4}}$ and $2^{\frac{1}{8}}$, the coefficients eventually maintain a consistent positive sign, thus indicating that the nearest singularity is on the positive real axis. We note that the consistent positive sign pattern was established only for higher-order coefficients; initially the sign alternated. This initial sign alternation apparently is attributable to the existence of further singularities, some of which are located off the real axis.

An estimate of the location of the singularities of the function $Nu(Ra^2)$ can be obtained by using Padé approximants (Baker 1965; Gaunt & Guttmann 1974). The term, 'Padé approximants', refers to the representation of functions like $Nu(Ra^2)$ as ratios of two polynomials, i.e.

$$Nu(Ra^2) = \frac{P_L(Ra^2)}{Q_K(Ra^2)} = \frac{\displaystyle\sum_{i=0}^{L} p_i \, Ra^{2i}}{1 + \displaystyle\sum_{i=1}^{K} q_i \, Ra^{2i}} \equiv \left[\frac{L}{K}\right], \tag{3.12}$$
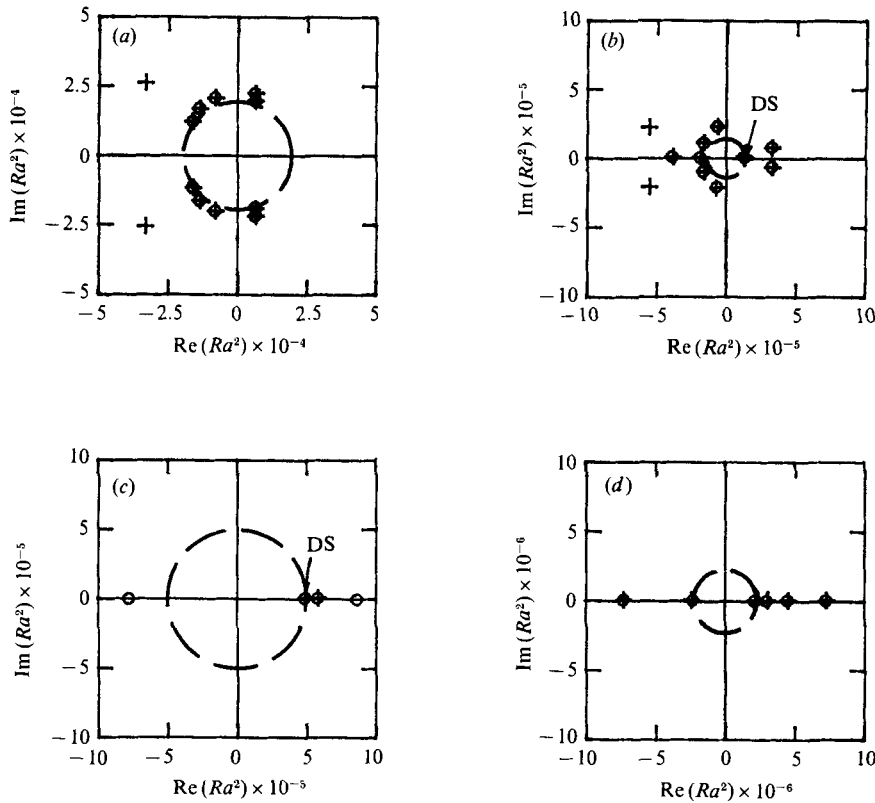
FIGURE 4. The location of the nearest singularities as predicted by the Padé approximation. (a) $R = 2$, (b) $2^{\frac{1}{2}}$, (c) $2^{\frac{1}{4}}$ and (d) $2^{\frac{1}{8}}$. The dashed circle denotes the disc of analyticity.

where the coefficients p_i and q_i can be uniquely determined in a straightforward fashion from the series expansion for $Nu(Ra^2)$ (Baker 1965). We note in passing that the Padé approximants can be used as an empirical means of analytically continuing series like (3.5) beyond the nearest singularity (Bau 1984). Here, we are merely interested in estimating the location of the singularities of the series (3.6). Information about the location of the singularities can be obtained by finding the poles and the zeros of the Padé approximants (3.12). Padé approximants are known (Gaunt & Guttmann 1974) to reproduce poles exactly and to simulate branch cuts by distributing poles and zeros along the cut. Usually, it is advantageous to consider the Padé approximants to the logarithmic derivative $[d/d(Ra^2)]$ $[\log Nu(Ra^2)]$ rather than to the function $Nu(Ra^2)$ itself since, in some cases, this transformation converts branch points into simple poles.

We calculated the poles and zeros of the Padé approximants [13/13], [14/14], [14/15] and [15/14] to the logarithmic derivatives. Poles that did not appear repetitively in all four approximations were assumed to be spurious and therefore were discounted. We depict the location of the poles nearest to the origin and the nearby zeros in the complex Ra^2 plane in figure 4. The poles and the zeros of the Padé approximants are denoted, respectively, by plus marks and circles. The dashed circle in figure 4 denotes the disc of analyticity.

For radii ratio $R = 2$ (figure 4a), the poles and zeros of the Padé approximants are off the real axis. It appears that the poles and zeros are distributed along a curve in

such a way that they simulate a branch cut. The Padé method suggests that the nearest singularity is off the real axis which is in line with the complicated sign pattern of the series' coefficients (table 1) and with the erratic behaviour of the Domb–Sykes' plot (figure 3a). The distance between the nearest singularity and the origin is estimated to be $Ra_c = 47 \pm 2$. This value has been used for the asymptote in figure 2(a). Since, in this case, the nearest singularity is off the real axis, it does not have any physical significance and thus is of little interest to us. Later, we shall see that, in addition to the complex singularity, the function $Nu(Ra^2)$ possesses a real singularity $Ra_1 \sim 62 > Ra_c$ such that for $Ra > Ra_1$, physically realizable multiple solutions do exist. (We adopt the convention that Ra_c and Ra_1 denote the distance to the *nearest* and the *nearest real* singularities, respectively.)

The Padé approximants fail to predict the existence of the real singularity at $Ra_1 \sim 62$. For radii ratios $R = 2^{\frac{1}{2}}$, $2^{\frac{1}{4}}$ and $2^{\frac{1}{8}}$, the nearest singularity lies on the positive real axis $(Ra_1 = Ra_c)$ (figure 4b–d). In all these cases, we observe a number of poles distributed along the real axis with zeros located almost at the pole locations. We hypothesize again that the zeros and poles of the Padé approximant are simulating a branch cut. For $R = 2^{\frac{1}{2}}$ and $2^{\frac{1}{4}}$, the distances between the nearest pole and and the origin are 119 and 223, respectively, and they are in very good agreement with the values predicted by the Domb–Sykes method (denoted by 'DS' in figure 4). For $R = 2^{\frac{1}{8}}$, the Padé method predicts $Ra_c = 472 \pm 5$ while the results of the Domb–Sykes test are not conclusive. We observe that for $R \leqslant 2^{\frac{1}{2}}$, the nearest singularity is real and therefore physically meaningful. We also note that in all the cases considered, there are additional singularities located off the real axis (not shown in figure 4c and d), which apparently are responsible for the sign alternations in the lower-order terms of the series (3.6) (see table 1). As higher-order terms in the series are computed (table 1), the nearest real singularity becomes dominating, a fact which is well reflected in the sign pattern of the series (table 1).

3.4. Generalized Euler transformations

Next, we shall attempt to diminish the effects of the non-real singularities by mapping them away. Our objective is to amplify the influence of the real singularities so as to improve the estimates provided by the Domb–Sykes' technique. To this end, we use the generalized Euler tranformation

$$u = \frac{z}{[(z-z_c)(z-z_c^*)]^{\frac{1}{2}}}, \tag{3.13}$$

where the complex-conjugate pair (z_c, z_c^*) represents the singularity we wish to map away. Here, $z = Ra^2$. The task at hand is to recast the series

$$Nu = \sum_{s=0}^{\frac{1}{2}S} N_s z^s$$

in terms of u, i.e.
$$Nu = \sum_{s=0}^{\frac{1}{2}S} b_s u^s. \tag{3.14}$$

This objective is conveniently accomplished by first expanding (3.13) into the series

$$u = \sum_{n=0}^{\infty} P_n(\cos \chi) \left(\frac{z}{\rho}\right)^{n+1} \tag{3.15}$$

R (M,N) s	2 (32,32)	$2^{\frac{1}{2}}$ (31,31)	$2^{\frac{1}{4}}$ (31,31)	$2^{\frac{1}{8}}$ (32,32)
0	$+1.0000\mathrm{E}+000$	$+1.0000\mathrm{E}+000$	$+1.0000\mathrm{E}+000$	$+1.0000\mathrm{E}+000$
1	$+3.7659\mathrm{E}-001$	$+49095\mathrm{E}-001$	$+4.2939\mathrm{E}-001$	$+4.1714\mathrm{E}-001$
2	$+5.0011\mathrm{E}-002$	$+2.5859\mathrm{E}-001$	$+2.5000\mathrm{E}-001$	$+2.5009\mathrm{E}-001$
3	$+1.6366\mathrm{E}-001$	$+1.8647\mathrm{E}-001$	$+1.8240\mathrm{E}-001$	$+1.8212\mathrm{E}-001$
4	$+4.5854\mathrm{E}-002$	$+1.4873\mathrm{E}-001$	$+1.4473\mathrm{E}-001$	$+1.4419\mathrm{E}-001$
5	$+1.0655\mathrm{E}-001$	$+1.3002\mathrm{E}-001$	$+1.2083\mathrm{E}-001$	$+1.2003\mathrm{E}-001$
6	$+3.9280\mathrm{E}-002$	$+1.2954\mathrm{E}-001$	$+1.0441\mathrm{E}-001$	$+1.0324\mathrm{E}-001$
7	$+7.5473\mathrm{E}-002$	$+1.8655\mathrm{E}-001$	$+9.3747\mathrm{E}-002$	$+9.1103\mathrm{E}-002$
8	$+3.3720\mathrm{E}-002$	$+5.0527\mathrm{E}-001$	$+9.1561\mathrm{E}-002$	$+8.1354\mathrm{E}-002$
9	$+5.8831\mathrm{E}-002$	$+2.1573\mathrm{E}+000$	$+1.3468\mathrm{E}-001$	$+7.6363\mathrm{E}-002$
10	$+3.3665\mathrm{E}-002$	$+1.0845\mathrm{E}+001$	$+5.1954\mathrm{E}-001$	$+6.4299\mathrm{E}-002$
11	$+5.3090\mathrm{E}-002$	$+5.7244\mathrm{E}+001$	$+4.3092\mathrm{E}+000$	$+1.4057\mathrm{E}-001$
12	$+3.7408\mathrm{E}-002$	$+3.0687\mathrm{E}+002$	$+4.6007\mathrm{E}+001$	$+5.0601\mathrm{E}-003$
13	$+5.0450\mathrm{E}-002$	$+1.6524\mathrm{E}+003$	$+5.6801\mathrm{E}+002$	$+5.8175\mathrm{E}+000$
14	$+3.7121\mathrm{E}-002$	$+8.8989\mathrm{E}+003$	$+7.7513\mathrm{E}+003$	$+2.1488\mathrm{E}+001$
15	$+4.2260\mathrm{E}-002$	$+4.7843\mathrm{E}+004$	$+1.1506\mathrm{E}+005$	$+9.6717\mathrm{E}+002$
16	$+2.8638\mathrm{E}-002$	$+2.5659\mathrm{E}+005$	$+1.8249\mathrm{E}+006$	$+1.1979\mathrm{E}+004$
17	$+2.9619\mathrm{E}-002$	$+1.3725\mathrm{E}+006$	$+3.0548\mathrm{E}+007$	$+3.5344\mathrm{E}+005$
18	$+2.0135\mathrm{E}-002$	$+7.3223\mathrm{E}+006$	$+5.3378\mathrm{E}+008$	$+7.8639\mathrm{E}+006$
19	$+2.4764\mathrm{E}-002$	$+3.8966\mathrm{E}+007$	$+9.6519\mathrm{E}+009$	$+2.4048\mathrm{E}+008$
20	$+2.4253\mathrm{E}-002$	$+2.0687\mathrm{E}+008$	$+1.7930\mathrm{E}+011$	$+7.3516\mathrm{E}+009$
21	$+3.4367\mathrm{E}-002$	$+1.0958\mathrm{E}+009$	$+3.4023\mathrm{E}+012$	$+2.5919\mathrm{E}+011$
22	$+3.7638\mathrm{E}-002$	$+5.7924\mathrm{E}+009$	$+6.5634\mathrm{E}+013$	$+9.7150\mathrm{E}+012$
23	$+4.3252\mathrm{E}-002$	$+3.0560\mathrm{E}+010$	$+1.2824\mathrm{E}+015$	$+3.9732\mathrm{E}+014$
24	$+3.7389\mathrm{E}-002$	$+1.6093\mathrm{E}+011$	$+2.5302\mathrm{E}+016$	$+1.7334\mathrm{E}+016$
25	$+2.8899\mathrm{E}-002$	$+8.4600\mathrm{E}+011$	$+5.0294\mathrm{E}+017$	$+8.0698\mathrm{E}+017$
26	$+1.2313\mathrm{E}-002$	$+4.4401\mathrm{E}+012$	$+1.0053\mathrm{E}+019$	$+3.9734\mathrm{E}+019$
27	$-1.5121\mathrm{E}-006$	$+2.3267\mathrm{E}+013$	$+2.0177\mathrm{E}+020$	$+2.0607\mathrm{E}+021$
28	$-7.0158\mathrm{E}-003$	$+1.2174\mathrm{E}+014$	$+4.0618\mathrm{E}+021$	$+1.1196\mathrm{E}+023$
29	$+1.1003\mathrm{E}-003$	$+6.3612\mathrm{E}+014$	$+8.1943\mathrm{E}+022$	$+6.3449\mathrm{E}+024$
30	$+2.0758\mathrm{E}-002$	$+3.3193\mathrm{E}+015$	$+1.6556\mathrm{E}+024$	$+3.7352\mathrm{E}+026$
z_c	$-750+2046i$	$-54666+21765i$	$-931368+220135i$	$-1.60\mathrm{E}7+2.30\mathrm{E}6i$

TABLE 2. The coefficients b_s in the modified series $Nu = \Sigma_{s=0}^{\frac{1}{2}S} b_s Ra^{2s}$. The numbers (M,N) indicate the level of truncation (3.4).

and subsequently reverting the series to obtain $z = z(u)$. In the above, P_n are Legendre polynomials and $z_c = \rho \exp(i\chi)$.

The resulting coefficients b_s of the modified series (3.14) are tabulated in table 2. The values of z_c which were used in the transformation are recorded at the bottom of the table. We observe that for the series corresponding to $R \leqslant 2^{\frac{1}{2}}$, all the coefficients are positive. This fact indicates that in these cases $R \leqslant 2^{\frac{1}{2}}$, we were successful in diminishing the effects of the complex singularities in the series (3.6). For $R = 2$, the results are not nearly as spectacular. The first 26 coefficients in the series are positive, but the sign pattern becomes erratic thereafter. We repeated the procedure for $R = 2$, using a variety of choices for z_c in (3.13). We also tried to map away simultaneously a number of singularities, but to no avail. Despite our efforts, we did not succeed in obtaining a consistent sign pattern for $R = 2$. From the data provided in table 2, however, we hypothesize that the function $Nu(Ra^2)$ for $R = 2$ may possess an additional real singularity $Ra_1 > Ra_c = 47$. We shall provide more support for this conjecture later in the paper.
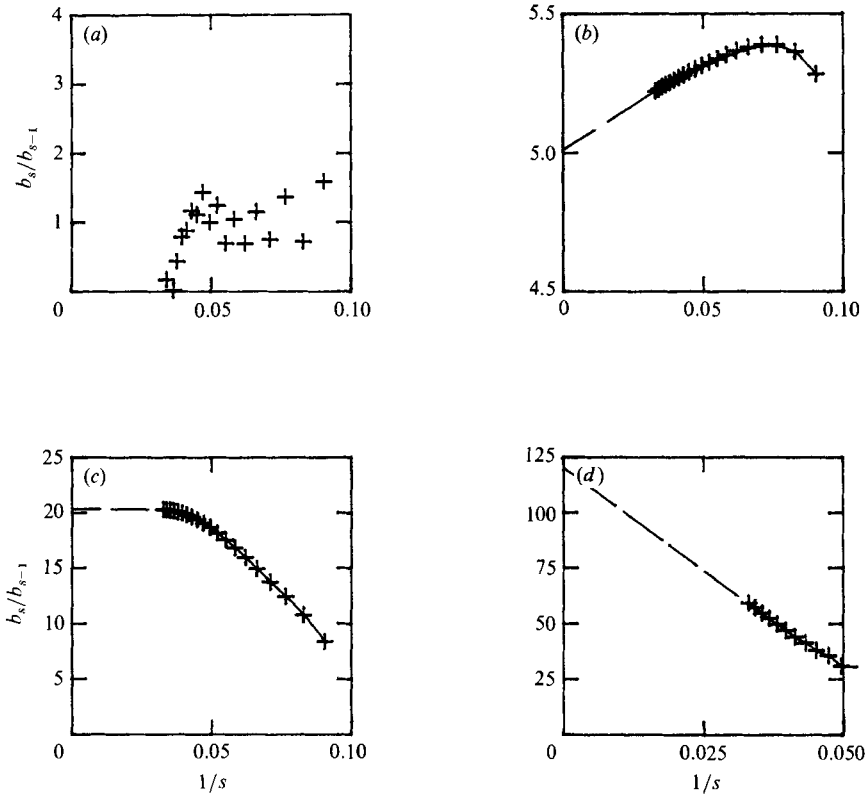
FIGURE 5. Domb–Sykes plots for the modified series (3.14). (a) $R = 2$, (b) $2^{\frac{1}{2}}$, (c) $2^{\frac{1}{4}}$ and (d) $2^{\frac{1}{8}}$.

Next, we depict in figure 5 the Domb–Sykes plots based on the coefficients of the modified series (equation (3.14), table 2). For $R = 2$, the Domb–Sykes plot (figure 5a) behaves erratically and does not provide any useful information. For $R \leqslant 2^{\frac{1}{2}}$, the Domb–Sykes curves of the modified series are better behaved than those of the original series (figure 3). For $R = 2^{\frac{1}{2}}$ and $2^{\frac{1}{4}}$, the predictions of the radius of convergence Ra_c are consistent with those reported in §3.2. For $R = 2^{\frac{1}{8}}$, linear extrapolation suggests $Ra_c \sim 364$ while the quadratic extrapolation yields erratic behaviour; thus we shall rely on the estimates obtained with the Padé method.

Before we conclude this section of the paper, we note in passing that while the generalized Euler transformation is useful in mapping away undesired singularities, it introduces at the same time new singularities into the modified series. These new singularities may be detected by analysing the singularities of the transformation (3.13). One needs to make sure that the new singularities are sufficiently far away from those which are under investigation.

3.5. A few concluding remarks about the series analysis

In this section we analyse an extended perturbation expansion in order to estimate the radius of convergence Ra_c and the nature of the nearest singularities of the series. The effective Rayleigh numbers $Ra_c^*(R-1)$ which correspond to the radius of convergence and the distance to the nearest real singularity $Ra_1^*(r-1)$ are depicted as a function of the radii ratio R by solid and dashed lines, respectively, in figure 6. We note in passing that as $R-1 \to 0$, $Ra_1^*(R-1) \to 4\pi^2$, which is the critical Rayleigh
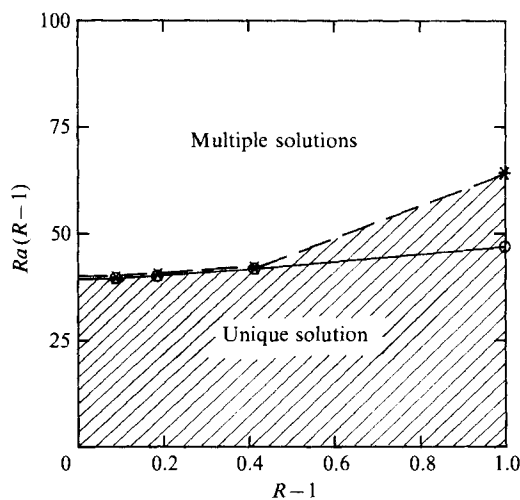
FIGURE 6. The radius of convergence (solid line) and the distance to the nearest real singularity (dashed line) are shown as a function of the radii ratio R. The shaded region corresponds to a region in which the DOB equations possess a unique solution.

number for the onset of convection (the first bifurcation) in a horizontal porous layer heated from below (Lapwood 1948). This, of course, is not coincidental. As $(R-1) \to 0$, the geometry at the top of the gap resembles that of an infinite layer. We shall see in §4 that in the case of the low radii ratios, this is the place where a secondary cell will evolve.

For $Ra < Ra_c$, the function $Nu(Ra^2)$ is analytic (Lang 1985), and therefore unique. Thus, it is likely that for $Ra < Ra_c$, the DOB equations possess a unique, two-dimensional, steady solution. For $Ra > Ra_c$, there may be multiple solutions. For radius ratio $R = 2$, the nearest singularity is complex; thus, the multiple solutions are not physically realizable. We shall see later that the series for $R = 2$ possesses an additional real singularity $Ra_1 \sim 62$ (denoted as * in figure 6), beyond which point physically realizable multiple solutions do exist. For radii ratios $R \le 2^{\frac{1}{2}}$, the nearest singularity is real, and we shall show that multiple solutions do, in fact, exist for $Ra > Ra_c$. The loss of uniqueness may occur as a result of either bifurcation or the appearance of isolated solution branches. In the next section, we investigate the nature of the muliple solutions for $Ra > Ra_1$.

4. Solution of the nonlinear problem

4.1. *The procedure*

In this section, we describe the solution of the nonlinear equations (2.2) using the Galerkin technique. The dependent variables ψ and T are expanded into the truncated Fourier series:

$$\left.\begin{aligned}
\psi(x,y) &\sim \sum_{n=1}^{N} \sum_{m=1}^{N-n+1} A_{m,n} \sin\left(\frac{m\pi x}{\log R}\right) \sin ny, \\
T(x,y) &\sim 1 - \frac{x}{\log R} + \sum_{n=1}^{N} \sum_{m=1}^{N-n+1} B_{m,n} \sin\left(\frac{m\pi x}{\log R}\right) \cos ny.
\end{aligned}\right\} \quad (4.1)$$

By substituting (4.1) into (2.2) and requiring that (2.2) is satisfied in the sense of weighted residuals, we convert the non-linear p.d.e.'s (2.2) into a set of o.d.e.'s which can be presented compactly as

$$\frac{\mathrm{d}\omega}{\mathrm{d}t} = \boldsymbol{S}^{-1}\boldsymbol{F}(\omega(Ra), Ra). \tag{4.2}$$

For notational as well as computational convenience, we map the two-dimensional matrix of unknowns $B_{m,n}$ onto the column vector $\omega(1 \times \frac{1}{2}(N+2)(N+1))$. In order to minimize the number of unknowns, we retain the explicit relationship between A_{ij} and B_{mn} as suggested by the linear momentum equation (2.2a). The vector $\boldsymbol{F}$ represents the right-hand side of (2.2b) while the square matrix $\boldsymbol{S}$ results from the non-constant coefficient of the time derivative in (2.2b). We shall refer to $\boldsymbol{S}$ as the 'shape' matrix. The explicit forms of $\boldsymbol{F}$ and $\boldsymbol{S}$ along with the explicit relationship between A_{ij} and B_{mn} are given in Appendix E.

We note in passing that for a fixed total number of spectral terms, the aforementioned truncation (4.1) led to a faster convergence than could be achieved by retaining N terms both in the x- and y-directions. This higher rate of convergence is attributable to the fact that the chosen truncation (4.1) allows one to incorporate higher-order harmonics than otherwise would be possible.

Steady-state solutions of (4.2) are found by solving the $\frac{1}{2}(N+1)(N+2)$ nonlinear algebraic equations

$$\boldsymbol{F}(\omega(Ra), Ra) = 0, \tag{4.3}$$

Our main objective is to compute the solution branch $\omega(Ra)$, which coincides for $Ra = 0$ with the no-motion solution ω_0. The procedure is briefly described below. Let us assume that we know a solution point, say $(\tilde{\omega}, \widetilde{Ra})$. If the Frechet derivative of $\boldsymbol{F}$ with respect to ω at the solution point, denoted here as $\tilde{\boldsymbol{F}}_\omega \equiv \boldsymbol{F}_\omega(\tilde{\omega}, \widetilde{Ra})$, is non-singular, the Implicit Function Theorem (Fulks 1961) guarantees a locally unique solution $(\omega(Ra), Ra)$. Thus starting from the known solution $(\tilde{\omega}, \widetilde{Ra})$, Newton's method provides the iteration

$$\omega = \tilde{\omega} - \tilde{\boldsymbol{F}}_\omega^{-1} \frac{\partial \boldsymbol{F}(\tilde{\omega}, \widetilde{Ra})}{\partial Ra}(Ra - \widetilde{Ra}). \tag{4.4}$$

Practicality considerations require us to use a finite increment $Ra - \widetilde{Ra}$. As a result, it is unlikely that the vector ω computed in (4.4) would satisfy (4.2) to a desired accuracy. Thus, we follow iteration (4.4) with a sequence of corrector steps in which Ra is fixed:

$$\omega_{i+1} = \omega_i - \boldsymbol{F}_\omega^{-1}(\omega_i, Ra)\boldsymbol{F}(\omega, Ra). \tag{4.5}$$

Sequence (4.5) is repeated until the desired accuracy is achieved. To this end, we use the convergence criteria:

$$\|\boldsymbol{F}\| \leqslant \epsilon, \quad \|\omega_{i+1} - \omega_i\|/\|\omega_i\| \leqslant \epsilon.$$

The procedure described above can be used as long as the Jacobian $\boldsymbol{F}_\omega$ in non-singular. Values of the Rayleigh number $Ra = Ra_c$ at which the determinant of the Jacobian ($|\boldsymbol{F}_\omega|$) vanishes are identified as possible bifurcation points or points at which the solution is no longer locally unique. In figure 7, we depict the Jacobian's determinant ($|\boldsymbol{F}_\omega|$) as a function of the Rayleigh number Ra for radii ratios $R = 2^{\frac{1}{2}}$ (figure 7a) and $R = 2^{\frac{1}{4}}$ (figure 7b).

4.2. The behaviour of the Jacobian as a function of the Rayleigh number

In figure 7(a), we depict $|\boldsymbol{F}_\omega|$ as a function of the Rayleigh number Ra for $R = 2^{\frac{1}{2}}$. Similar qualitative behaviour (not shown here) was observed for $R = 2$.
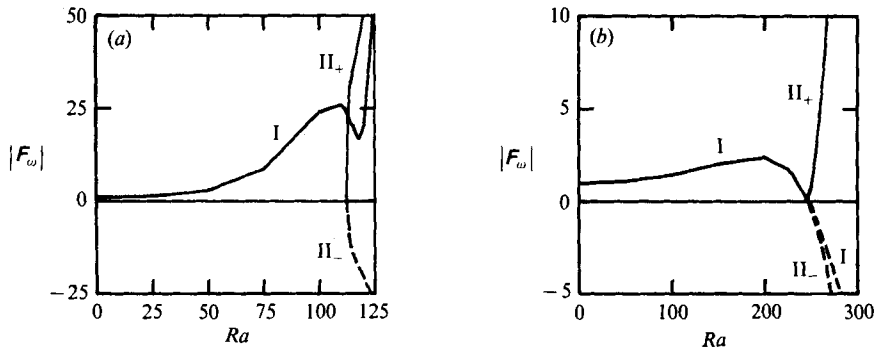
Figure 7. The Jacobian's determinant ($|\mathbf{F}_\omega|$) depicted as a function of the Rayleigh number Ra. (a) $R = 2^{\frac{1}{2}}$, and (b) $2^{\frac{3}{4}}$.

The solution branch which corresponds to the no-motion solution is denoted I in figure 7 (a). For $Ra = 0$, $|\mathbf{F}_\omega| = 1$. As the Rayleigh number increases, the magnitude of the Jacobian increases, although not monotonically. At $Ra \sim 120$, $|\mathbf{F}_\omega|$ dips and then picks up again. Before the dip, the flow structure consists of bicellular flow which we refer to as 2-C structure (figure 11a). Beyond the dip, the flow becomes multicellular (figure 11b and c). The transition from one flow regime to another is smooth and does not involve a bifurcation. Note that the Jacobian in branch I does not become singular in the range of Rayleigh numbers considered here.

We also detected a second solution branch, which we call II in figure 7 (a). This solution branch is an isolated one, which exists only for $Ra > Ra_c \sim 112$. Branch II has a turning point at $Ra = Ra_c$. The lower half of the branch II$_-$ is unstable and thus is depicted with a dashed line, while the upper half II$_+$ is stable. In this paper, we adopt the convention that linearly stable solutions are shown with solid lines while unstable solutions are shown with dashed lines. We shall discuss the linear stability analysis later in this section. The lower half II$_-$ corresponds to a 2-C flow structure (figure 11d) while the upper half II$_+$ corresponds to a multicellular structure (figure 11e and f). Both branches I and II$_+$ eventually lose stability via a Hopf bifurcation at $Ra \sim 200$ and $Ra \sim 490$, respectively. We note in passing that we traced solution branch II through the turning point by considering the Rayleigh number in (4.3) to be an unknown and regarding one of the unknowns in ω as a controlling parameter.

In figure 7 (b) we depict $|\mathbf{F}_\omega|$ as a function of Ra for $R = 2^{\frac{3}{4}}$. Similar qualitative behaviour (not shown here) was exhibited in the case of $R = 2^{\frac{5}{8}}$.

The solution branch which corresponds to the no-motion solution ($|\mathbf{F}_\omega| = 1$ at $Ra = 0$) is denoted as I. As the Rayleigh number increases, the determinant $|\mathbf{F}_\omega|$ initially increases in magnitude; but eventually this trend changes. The determinant starts to decline, crosses the zero axis at $Ra = Ra_c \sim 245$ (for truncation level $N = 19$) and then assumes negative values. At the bifurcation point, the solution branch loses stability (a fact which is denoted by a dashed line in figure 7b).

At the first bifurcation point, $Ra = Ra_c$, a second solution branch, which we denote as II, intersects with the primary branch I. The second branch also possesses a turning point at Ra_c. The upper half of the branch II$_+$ corresponds to a stable multicellular structure (figure 13c–f) while the lower half of the branch II$_-$ corresponds to a 2-C (figure 13b) unstable structure. Newton's method allows us to cross the bifurcation point ($|\mathbf{F}_\omega| = 0$) without difficulty as long as points too close are not used. The point $Ra = Ra_c$ can be obtained using the method of bisection, for

example. Plots like figure 7 are useful for obtaining some insights into the behaviour of the Jacobian as a function of the Rayleigh number. However, in general one can compute the singular point Ra_c directly by adding an additional equation to set (4.3) and treating Ra as an unknown. This gives us

$$\left.\begin{array}{l} \boldsymbol{F}(\omega, Ra) = 0, \\ \text{Det}\,(\boldsymbol{F}_\omega(\omega, Ra)) = 0. \end{array}\right\} \quad (4.6)$$

Additionally, we were able to cross the bifurcation point by employing the cord technique (Decker & Keller 1980).

We briefly summarize our results up to this point. Clearly, there exists some critical Rayleigh number Ra_c beyond which the DOB equations possess multiple solutions. For $R = 2$ and $2^{\frac{3}{4}}$, the additional solutions appear as isolated branches while for $R = 2^{\frac{1}{4}}$ and $2^{\frac{1}{8}}$, these solutions appear through a bifurcation process. Of course, there is no guarantee that we have found all possible solutions for $Ra > Ra_c$.

4.3. *Linear stability*

The linear stability of any solution branch can be readily obtained by computing the eignevalues of the matrix $(\boldsymbol{S}^{-1}\boldsymbol{F}_\omega)$. Eigenvalues with negative or positive real parts indicate, respectively, linearly stable and unstable solutions. Of particular interest is the eigenvalue with the largest real part. We denote the magnitude of the real part of this eigenvalue by Max (λr).

For illustration purposes, we depict in figure 8 Max (λr) as a function of the Rayleigh number for $R = 2^{\frac{3}{4}}$. It turns out that for $Ra < 610$, this eigenvalue is real. First, we shall focus our attention on solution branch I (figure 7b). For $Ra < Ra_c$, Max $(\lambda r) < 0$, which indicates that the 2-C structure is linearly stable. At the bifurcation point $(Ra = Ra_c)$, Max $(\lambda r) = 0$, and for $Ra > Ra_c$, Max $(\lambda r) > 0$. This is consistent with the Jacobian's determinant changing sign at $Ra = Ra_c$ (figure 7b). The 2-C structure (branch I) loses stability at the bifurcation point. In figure 8, we denote stable and unstable solutions by solid and dashed lines, respectively.

At the bifurcation point, two additional families of solutions are generated, II$_+$ and II$_-$ (see also figure 7b). The Max (λr) corresponding to II$_+$ is negative which indicates linear stability. Max $(\lambda r) > 0$ for the II$_-$ solution which indicates that this solution is unstable.

In sum, thus far we have observed that, for $Ra < Ra_c$, the solution of the flow field is of the 2-C type. At $Ra = Ra_c$, this solution I loses stability and another steady-state solution II$_+$ of the multicellular type gains stability. This indicates that Ra_c is a bifurcation point. In fact, by the Leray–Schauder theory, we were guaranteed that $Ra = Ra_c$ would be such a bifurcation point since Max (λr) is an eigenvalue of odd multiplicity (a simple eigenvalue in our case).

We note in passing that for the branch II$_+$, for some $Ra > Ra_c$, the eigenvalue with the largest real part becomes complex. In fact, the branch II$_+$ undergoes Hopf bifurcation at $Ra \sim 610$.

Similar types of calculations also were carried out for the other radii ratios, providing us with the necessary information with respect to the stability of the various solution families.

4.4. *The effects of truncation*

A matter of great concern to us was the effect of the truncation level (N in (4.1)) on both the qualitative and quantitative nature of our results. To this end, we repeated
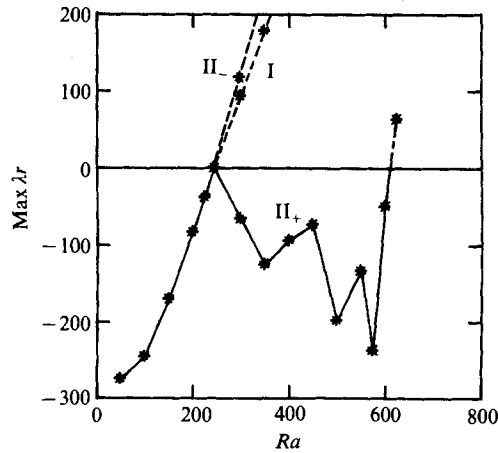
FIGURE 8. The maximum eigenvalue of the matrix $(S^{-1}F_\omega)$ is shown as a function of the Rayleigh number Ra for $R = 2^{\frac{1}{4}}$.
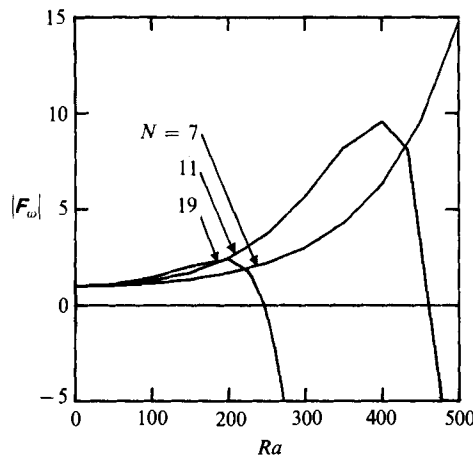

FIGURE 9. The effect of the truncation level N on the qualitative behaviour of the Jacobian's determinant as a function of the Rayleigh number for $R = 2^{\frac{1}{4}}$.

our calculations for various values of N. As an illustration, we depict in figure 9 for $R = 2^{\frac{1}{4}}$, the behaviour of the Jacobian as a function of the Rayleigh number for various truncation levels, N. It turns out that for $N < 11$, no bifurcations occur at all in the range considered. The Jacobian's determinant keeps increasing indefinitely. For $N \geqslant 11$, we obtain a bifurcation at $Ra = Ra_c$. The magnitude of Ra_c, however, depends on N. As N increases, Ra_c decreases. Using the Galerkin technique, we predicted the critical Rayleigh numbers at which multiple solutions appear. They are denoted $Ra_{cG}(N)$. The corresponding values obtained by extrapolating the results to $N \to \infty$ are denoted by $Ra_{c\infty}$. We denote with E the relative difference between Ra_{cG} (N) and $Ra_{c\infty}$. That is,

$$E = \frac{Ra_{cG}(N) - Ra_{c\infty}}{Ra_{c\infty}}. \tag{4.7}$$
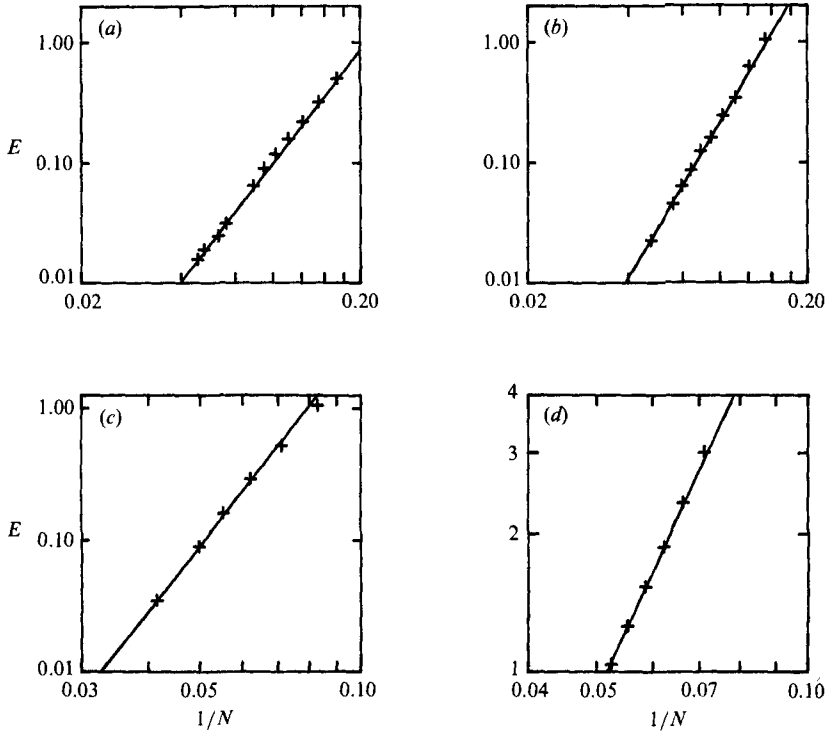
FIGURE 10. The effect of the truncation level N on the value Ra_{cG} beyond which multiple solutions exist. (a) $R = 2$, (b) $2^{\frac{1}{2}}$, (c) $2^{\frac{1}{4}}$ and (d) $2^{\frac{1}{8}}$.

E is depicted as a function of N in figure 10 for $R = 2$, $2^{\frac{1}{2}}$, $2^{\frac{1}{4}}$ and $2^{\frac{1}{8}}$. We observe that for a sufficiently large N, E behaves as a function of N in the following manner:

$$E = \left(\frac{a}{N}\right)^{\gamma}, \quad \gamma > 0, \tag{4.8}$$

where a and γ are constants which depend on the radii ratio R. Clearly, as $N \to \infty$, $E \to 0$. We note in passing that the computational time for computing Ra_c increases very fast with N, and it may not be practical to repeat the same calculations for a large number of cases. Instead, one may use (4.8) to extrapolate the results of the computations to $N \to \infty$. For $R = 2$, $2^{\frac{1}{2}}$, $2^{\frac{1}{4}}$ and $2^{\frac{1}{8}}$, we estimate $Ra_{c\infty} = 62$, 112, 224 and 470, which are in good agreement with the corresponding values obtained in §3.

5. Results and discussion

5.1. Comparison of the series analysis (§3) and the numerical solution (§4) – a region of uniqueness

In §3 we obtained a power series solution in terms of the Rayleigh number Ra for the temperature and flow fields and for the Nusselt number Nu.

In what follows, we focus on the series solution for the Nusselt number $Nu = \sum N_s Ra^{2s}$. This series has a finite radius of convergence since the function $Nu(Ra^2)$ has singularities in the complex Ra^2 plane.

On occasion, such as in the case of radii ratio $R = 2$, the nearest singularity lies off the real axis and thus has no physical significance. This singularity unnecessarily limits the range of utility of the series. One can use a variety of analytic continuation techniques (see, for example, Bau 1984) to extend the range of utility of the series beyond the non-real singularity. We mapped away the non-real singularity in an attempt to discover whether any additional real singularities existed. Although the modified series (3.14) could not predict a real singularity, it did indicate to us that such a singularity may exist. The analysis of §4 reveals that, indeed, there is a singularity at $Ra \sim 62$. For $Ra > 62$, multiple solutions exist. For radii ratios $R \leqslant 2^{\frac{1}{2}}$, the series analysis of §3 reveals that the nearest singularities lie on the positive real axis of the Ra^2 plane. For each of the series considered, the singularity is physically meaningful and it indicates the existence of a branch point beyond which the solution is not unique any more. This is confirmed in §4, where we solved the full nonlinear DOB equations. It turns out that for $R = 2^{\frac{1}{2}}$, the loss of uniqueness occurs as a result of the appearance of an isolated solution branch (figure 7a), while for $R = 2^{\frac{1}{4}}$ and $2^{\frac{1}{8}}$, the loss of uniqueness occurs as a result of a bifurcation process.

These results are summarized in figure 6, where the shaded area denotes the region of uniqueness for the two-dimensional, steady DOB equations in the parameter space (Ra, R).

5.2. *The flow and temperature fields*

In this section, we describe the structure of the flow and temperature fields which corresponds to the solution branches identified in §4.

The flow and temperature fields for $R = 2^{\frac{1}{2}}$ and $2^{\frac{1}{4}}$ are depicted, respectively, in figures 11 and 13 as functions of the Rayleigh number. The left-hand side of figures 11 and 13 depicts equally spaced isotherms while the right-hand side depicts the streamlines. In order to be able to show the weaker secondary convection, we had to dispense with showing the streamline in equally spaced fashion. Figures 12 and 14 depict the extreme values of the stream function as a function of the Rayleigh number.

In what follows, we shall first discuss radii ratios $R = 2$ and $2^{\frac{1}{2}}$ and then, $R = 2^{\frac{1}{4}}$ and $2^{\frac{1}{8}}$.

The structure of the flow field for $R = 2^{\frac{1}{2}}$ is depicted in figure 11 as a function of the Rayleigh number. Similar qualitative behaviour was observed for $R = 2$. Owing to space limitations, we do not depict the case of $R = 2$ here. The information is available in Himasekhar (1987).

We start our discussion by tracing the solution branch I which for $Ra = 0$ coincides with the conduction solution (see also figure 7a). For $0 < Ra < 120$, this solution branch I consists of two counter-rotating cells, one cell in each half of the annulus (figure 11a). That is, fluid is rising next to the hot inner cylinder and descending next to the outer, cold cylinder. The temperature field inside the annulus does not deviate significantly from the conductive (no-motion) temperature field. This is reflected by the isotherms being almost parallel to each other. As the Rayleigh number increases so does the intensity of the circulation. This fact is indicated by the increase in the extreme value of the stream function (ψ_{ext}) which appears as a monotonically increasing function of the Rayleigh number in figure 12. For $Ra > 120$, the flow structure becomes multicellular with the number of cells increasing from four (figure 11b) to six (figure 11c) as the Rayleigh number increases. The transition from a two-cell structure (2-C) into a multicellular structure occurs without bifurcation. The transition point coincides with the local minimum in the Jacobian's determinant (figure 7a); however, it is possible that this has no special significance. The extreme
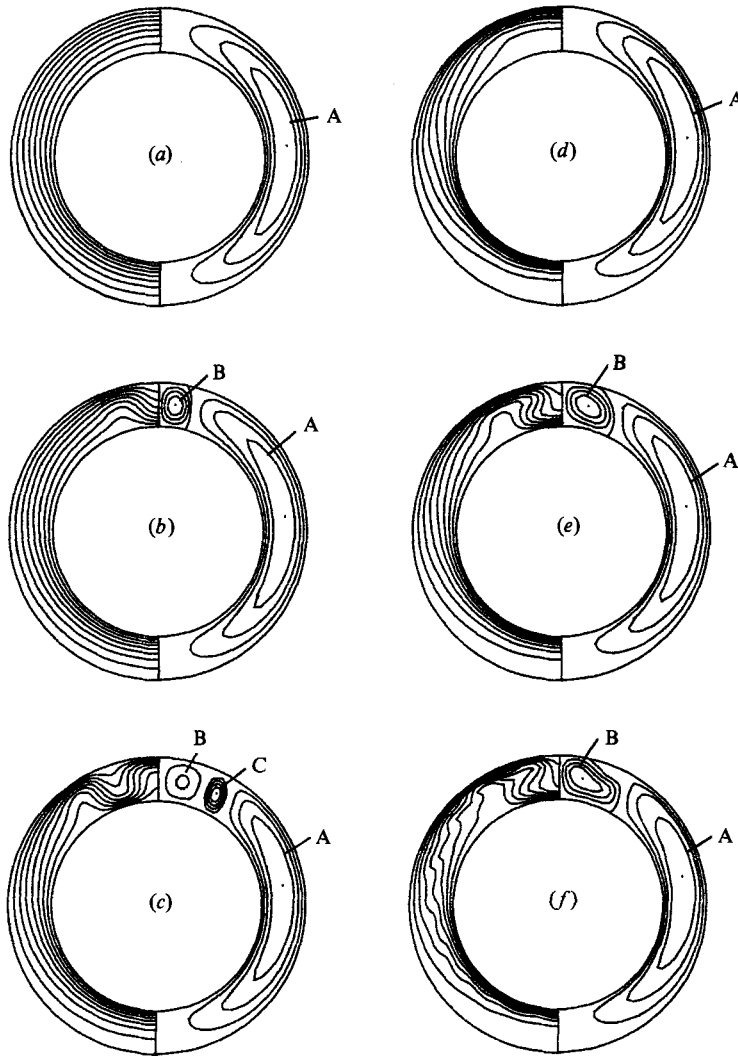
FIGURE 11. Flow and temperature fields for $R = 2^{\frac{1}{2}}$. The left-hand side and right-hand side of the figure depict the isotherm and the streamlines, respectively. (a) Branch I, $Ra = 100$, stable. (b) Branch I, $Ra = 125$, stable. (c) Branch I, $Ra = 195$, stable. (d) Branch II_, $Ra = 400$, unstable. (e) Branch II_+, $Ra = 300$, stable. (f) Branch II_+, $Ra = 500$, unstable (oscillatory).

values of the stream functions associated with the secondary circulation are depicted in figure 12. Capital letters A, B, etc. are assigned to the various cells to allow cross reference between figures 11 and 12. As is evident from figure 12, the circulation associated with the secondary cells (B and B and C in figure 11b and c, respectively) is much weaker than the one associated with the primary cell A. Also, the convective cells are counter-rotating, i.e. the motions associated with cells A and B in figure 11b are, respectively, clockwise and counter-clockwise. As the Rayleigh number is further increased, solution branch I loses stability at $Ra \sim 200$ via a Hopf bifurcation. That is, at $Ra \sim 200$, the real parts of two complex-conjugate eigenvalues of the matrix $(\mathbf{S}^{-1}\mathbf{F}_{\omega})$ become positive.

Solution branch I is unique only for $Ra < 112$. For $Ra > 112$, we observe the
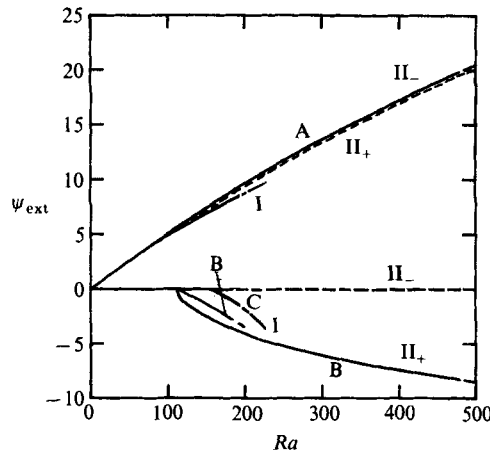
FIGURE 12. The extreme values of the stream function (ψ_{ext}) are depicted as a function of the Rayleigh number for $R = 2^{\frac{1}{2}}$. The capital letters allow cross-reference with figure 11.

appearance of an isolated branch which we denoted as II in figure 7(a). The upper half of the branch II_+ (figure 7a) is stable and the flow structure consists of four convective cells, two in each half of the annulus (figure 11e). As the Rayleigh number increases beyond about 490, solution branch II_+ loses stability via a Hopf bifurcation. The unstable solution is depicted in figure 11(f) for $Ra = 500$. The wiggly behaviour of the isotherms in figure 11(f) may indicate that an insufficient number of spectral terms was used in the computations. Thus, our conclusion about the location of the Hopf bifurcation should be considered a tentative one. We did not pursue this point any further owing to the expense associated with the incorporation of a larger number of spectral terms and the fact that our prime interest in this paper is the study of the flow structure around $Ra \sim Ra_c$.

The lower half of branch II, denoted as II_-, (figure 7a) is unstable from the very start (that is, the matrix $S^{-1}F_\omega$ posesses a real, positive eigenvalue). This solution branch represents a bicellular flow structure (figure 11d) which is very similar in appearance to branch I (for $Ra < 120$).

We conclude this subsection by noting that for $R = 2^{\frac{1}{2}}$ and $Ra > Ra_c = 112$, the DOB equations possess at least two stable steady solutions: namely branches I and II_+. A similar situation was observed for $R = 2$, $Ra > 62$.

Next, we describe the flow and temperature fields of the various solution branches associated with $R = 2^{\frac{1}{4}}$. Qualitatively similar behaviour was observed for $R = 2^{\frac{1}{8}}$. Owing to space limitations, we do not discuss the $R = 2^{\frac{1}{8}}$ case here in any detail. The interested reader is referred to Himasekhar (1987) for further details.

We start the discussion by tracing solution branch I, which coincides with the conductive solution for $Ra = 0$ (see also figure 7b). For $0 < Ra < Ra_c$, solution branch I consists of two counter-rotating cells (figure 13a). As Ra exceeds $Ra_c = 224$, this solution branch loses stability (one of the real eigenvalues of the matrix $S^{-1}F_\omega$ becomes positive). A new steady-state solution appears (figure 7b). We denote this new solution branch as II. Solution branch II has a turning point at $Ra = Ra_c$. The upper half of the branch is stable and consists initially of four convective cells (figure 13c). As the Rayleigh number increases so does the number of cells (figure 13d–f). Note that this further increase in the number of cells occurs without bifurcation (see also figure 7b). At about $Ra \sim 610$, branch II_+ loses stability via a Hopf bifurcation.
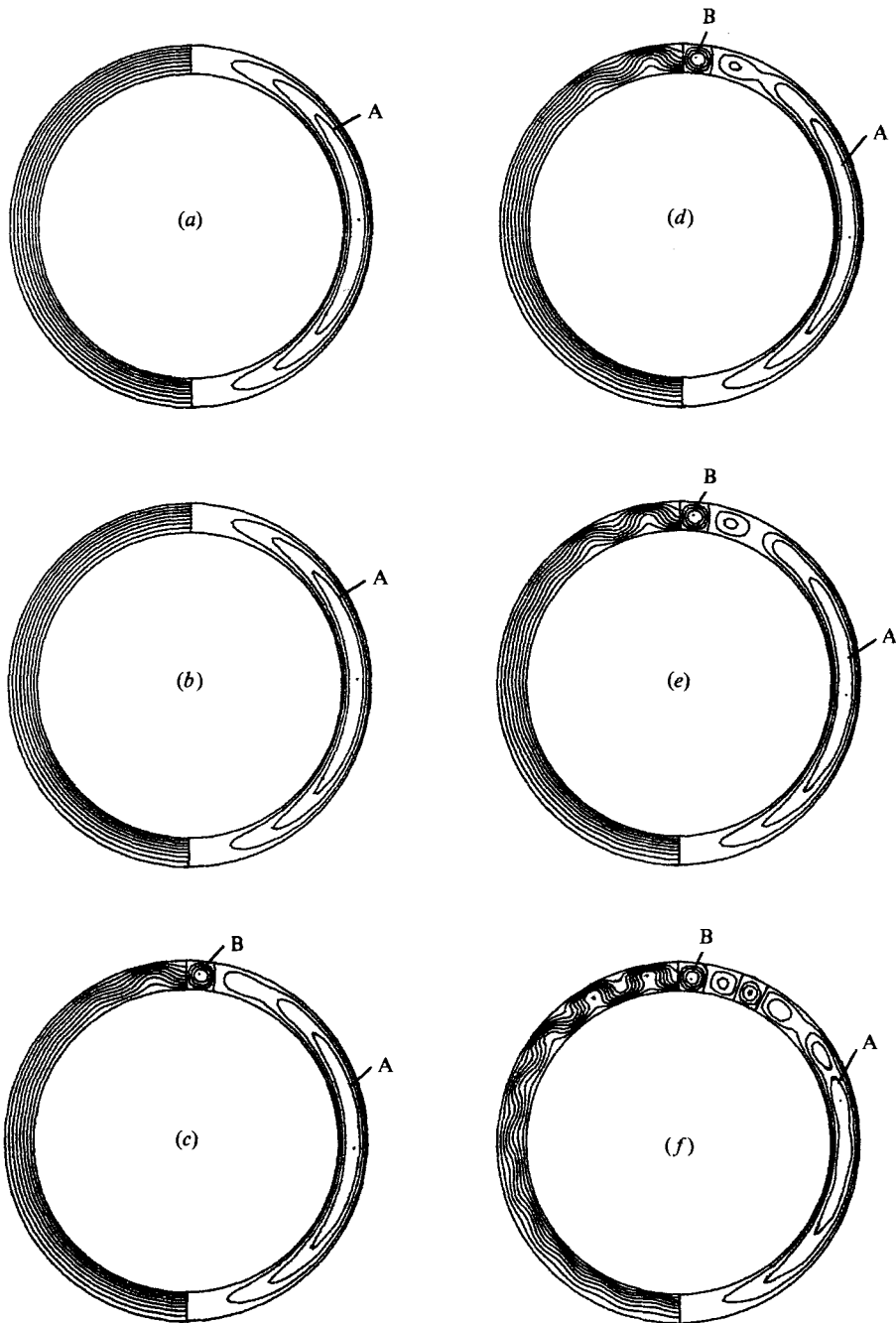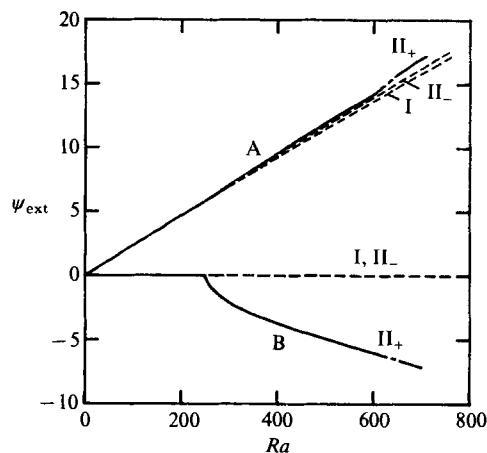
FIGURE 13. Flow and temperature fields for $R = 2^{\frac{1}{4}}$. The left-hand side and right-hand side of the figure depict the isotherms and the streamlines, respectively. (a) Branch I, $Ra = 200$, stable. (b) Branch II_-, $Ra = 270$, unstable. (c) Branch II_+, $Ra = 270$, Stable. (d) Branch II_+, $Ra = 295$, stable. (e) Branch II_+, $Ra = 315$, stable. (f) Branch II_+, $Ra = 500$, stable.

FIGURE 14. The extreme values of the streamfunction (ψ_{ext}) are depicted as a function of the Rayleigh number for $R = 2^{\frac{1}{4}}$. The capital letters allow cross-reference with figure 13.
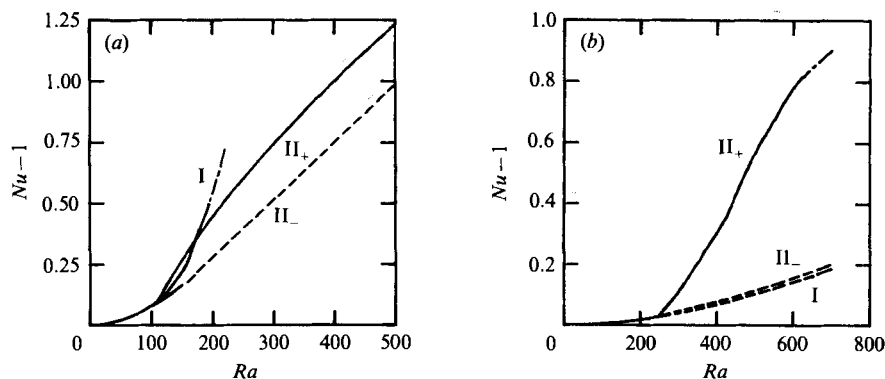
FIGURE 15. The Nusselt number Nu depicted as a function of the Rayleigh number Ra for (a) $R = 2^{\frac{1}{2}}$ and (b) $2^{\frac{1}{4}}$.

The lower half of solution branch II_- is unstable from the very outset (the matrix $S^{-1}F_\omega$ has a positive real eigenvalue). The flow structure associated with II_- is similar to the one associated with branch I (figure 13b).

The extreme values of the stream function as a function of the Rayleigh number are depicted in figure 14. To allow cross-referencing between figures 13 and 14, we denoted the extreme values of the stream function associated with the various cells by capital letters. Here again, the circulation associated with the secondary cells (B in figure 13) is much weaker than the one associated with the primary cell A.

5.3. The heat transfer

A matter of some practical interest is the magnitude of the heat transfer associated with the various solution branches. In figure 15(a, b), we depict the Nusselt number as a function of the Rayleigh number for $R = 2^{\frac{1}{2}}$ and $2^{\frac{1}{4}}$. Qualitatively similar behaviour was observed but not shown here for $R = 2$ and $2^{\frac{1}{8}}$. Stable and unstable solutions are shown, respectively, by solid and dashed lines.

For radii ratios $R \leqslant 2^{\frac{1}{4}}$ (figure 15b), the stable solution branches II_+ beyond the

bifurcation point have higher rates of heat transport than do the unstable solutions. The same, however, is not true for the isolated solutions which appear for $R \geqslant 2^{\frac{1}{2}}$ (figure 15a). In that case, branch I has the highest rate of heat transfer beyond its range of stability.

For a fixed Rayleigh number, the flow structures which consist of a larger number of convective cells mandate a higher rate of heat transfer. This may be attributed to the fact that an increase in the number of convective cells leads to a decrease in the circumferential length in which each packet of fluid is in contact with the hot boundary.

5.4. *Energy of the system*

Next, we compare the energy content of the various solution branches. We compute the energy contents in order to determine whether stable solutions have lower energy contents than do unstable ones. In other words, we are asking whether the selection of stable and unstable branches can be determined according to a 'minimal energy principle'. Since the contribution of the kinetic energy is negligible, we do not include it in our calculations. The total energy of the system per unit axial length may be approximated by

$$E_H = \iint \left(T_c \, r \, dr \, d\theta + \iint (T - T_c) \, r \, dr \, d\theta, \right. \tag{5.1}$$

where the thermal energy E_H is normalized with $\rho C_p (\hat{T}_i - \hat{T}_o) \, \hat{r}_i^2$. The value $E_H = 0$ is assigned to a system maintained at the temperature of the outer boundary ($\hat{T}_o$). The first term on the right-hand side represents the energy associated with a purely conductive state ($E_{H,c}$) while the second term represents the correction due to motion (ΔE_H). T_c in (5.1) is the conductive temperature distribution. Hence, we can write

$$E_H = E_{H,c} + \Delta E_H. \tag{5.2}$$

We depict ΔE_H as a function of the Rayleigh number for the various solution branches for $R = 2^{\frac{1}{2}}$ and $2^{\frac{1}{4}}$ which appear in figures 16 (a and b), respectively. The cases of $R = 2$ and $2^{\frac{1}{8}}$ are not shown here, but the qualitative behaviour is similar to that depicted in figures 16 (a and b), respectively. From figures 16 (a and b), it is evident that at and beyond the bifurcation and turning points, the stable solution branches possess lower energy content than do the unstable ones.

5.5. *Entropy generation*

Another quantity of physical interest is the rate of entropy generation associated with each of the solution branches. Thus, a calculation is carried out to investigate whether a principle of 'maximum entropy generation' exists. That is, we want to know whether stable solutions have a higher rate of entropy generation than do unstable ones. We calculate the non-dimensional entropy generation per unit axial length of the annulus (Bejan 1984, p. 355) as:

$$\dot{S}_g = \iint \left[\frac{\nabla T \cdot \nabla T}{T^2} + Ra^{-1} D \, \nabla \psi \cdot \nabla \psi \right] r \, dr \, d\theta, \tag{5.3}$$

where the integration is carried out over the cross-section's area. In the above, the entropy is scaled with the equivalent thermal conductivity of the medium k_{eq}. $D = \beta g r_i / C_p$ is the dissipation number.

Since (5.2) includes the absolute temperature, it was necessary to specify fluid and medium properties in order to facilitate numerical computation of $\dot{S}_g$. For illustration purposes, we assume that the working fluid is water with an average temperature of
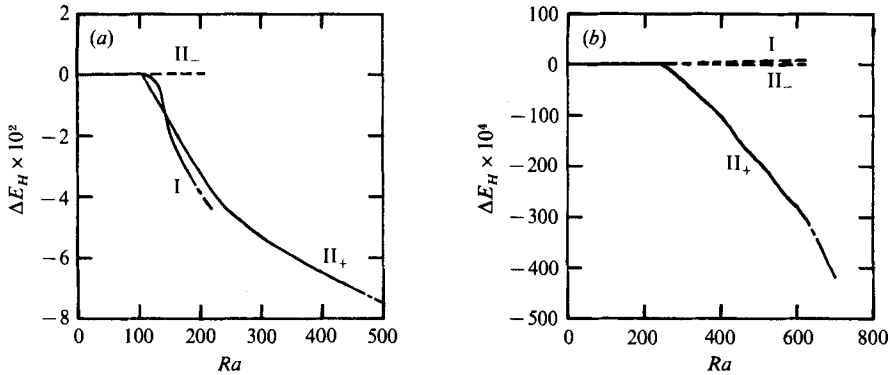
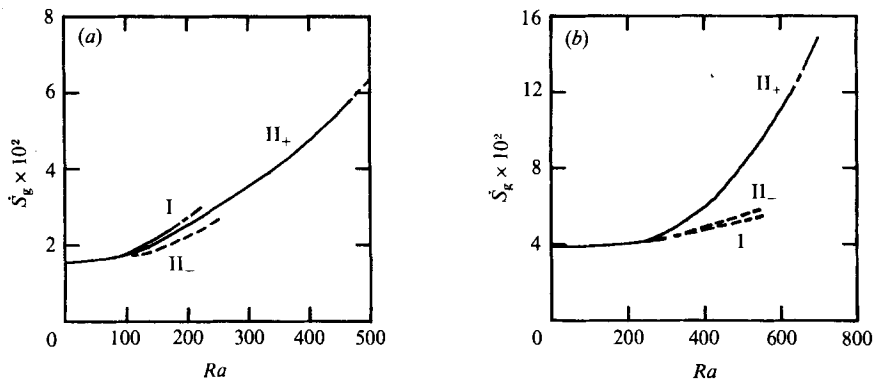FIGURE 16. Energy content of various solution branches depicted as a function of the Rayleigh number of (*a*) $R = 2^{\frac{1}{2}}$ and (*b*) $2^{\frac{1}{4}}$.

FIGURE 17. Entropy generation rate associated with various solution branches for (*a*) $R = 2^{\frac{1}{2}}$, and (*b*) $2^{\frac{1}{4}}$.

20 °C, $\hat{T}_i - \hat{T}_0 = 10$ °C, the medium's permeability is $\kappa = 10^{-8}\,\text{m}^2$, and the radius $r_i = 0.15$ m. The corresponding dissipation number $D = 7.3 \times 10^{-8}$.

The entropy generation rate of the various solutions as a function of the Rayleigh number is depicted in figures 17 (*a* and *b*) for $R = 2^{\frac{1}{2}}$ and $2^{\frac{1}{4}}$, respectively. The cases of $R = 2$ and $R = 2^{\frac{1}{8}}$, though not shown here, are qualitatively represented by figures 17 (*a* and *b*), respectively. We observe that beyond bifurcation and turning points the stable solution branches possess higher rates of entropy generation than do the unstable ones.

5.6. *Stability*

Finally, our results allow us to depict a 'stability' curve. In figure 18, we show the various two-dimensional flow structures in the (Ra, R)-plane. We focus only on those solutions which for $Ra = 0$ coincide with the conduction solution. The area beneath the lower curve corresponds to steady, bicellular convection. Once the magnitude of the Rayleigh number exceeds the lower curve, the flow structure becomes multicellular. For $R < 2^{\frac{1}{2}}$, the transition occurs via bifurcation while for $R > 2^{\frac{1}{4}}$, it occurs smoothly without bifurcation. As $R \to 1$, $Ra(R-1) \to 4\pi^2$, which is the Rayleigh-number value of the first bifurcation in the infinite, horizontal porous layer (Lapwood 1948). As the Rayleigh number is further increased, the multicellular structure loses stability via a Hopf bifurcation and the flow becomes oscillatory. For
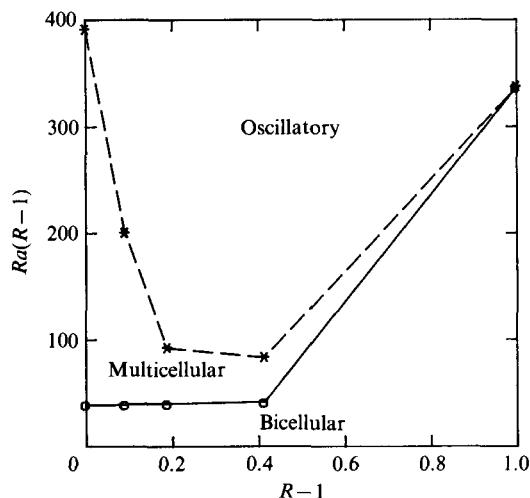
FIGURE 18. A schematic stability curve for type I solutions in a two dimensional setting.

$R \to 1$, we depict in figure 18, the value of the Rayleigh number (390.7) which corresponds to a Hopf bifurcation in a horizontal, infinite porous layer (Aidun & Steen 1987). Clearly, the latter is consistent with the trends observed in our own computations. The isolated solution branches observed for $R \geqslant 2^{\frac{1}{2}}$ are not depicted in figure 18.

The results stated thus far certainly apply to a narrow annulus ($A \ll 1$). Such a situation may exist, for example, in a Hele–Shaw cell. Next, we shall comment on the applicability of our results in situations in which the aspect ratio, A, is not small. In such situations, both three- and two-dimensional bifurcations are possible. Indeed, Caltagirone (1976) has studied a similar problem to the one presented in this paper. While he has not observed any two-dimensional bifurcations such as those reported here, he has observed that the bicellular solution undergoes a Hopf bifurcation into a three-dimensional, time-dependent solution. It appears, therefore, that the bicellular flow structure may undergo one of two types of bifurcations, i.e. into either a multicellular two-dimensional structure or a three-dimensional, time-dependent structure.

To determine which of these bifurcations will occur in practice, we plot with a dashed line Caltagirone's (1976) stability curve for aspect ratios $A = \infty$ and $A = 0.5$ (see figure 19). The solid line corresponds to our own results pertaining to two-dimensional bifurcations of the 'conductive' (type I) solutions. The curve for $A = 0.5$ is not given explicitly by Caltagirone. He only computed the effect of axial confinement A for $R = 2$. The curve for $A = 0.5$ was constructed assuming that a similar relative effect applies to other radii ratios as well. The area above the dashed line indicates three-dimensional, unsteady flow. For an infinitely long horizontal annulus in which $R \geqslant 2^{\frac{1}{4}}$, the bicellular solution will bifurcate into a three-dimensional unsteady solution and the two-dimensional, multicellular solution will never be observed in practice. When $R \leqslant 2^{\frac{1}{4}}$, the values predicted by Caltagirone (1976) for three-dimensional bifurcation are very close to our own. Unfortunately, the precision of both of these calculations does not allow us to predict with certainty which type of bifurcation will occur. It is quite plausible that for $R < 2^{\frac{1}{4}}$ and $A = \infty$, the two-dimensional, multicellular mode will be the preferred one. This view is
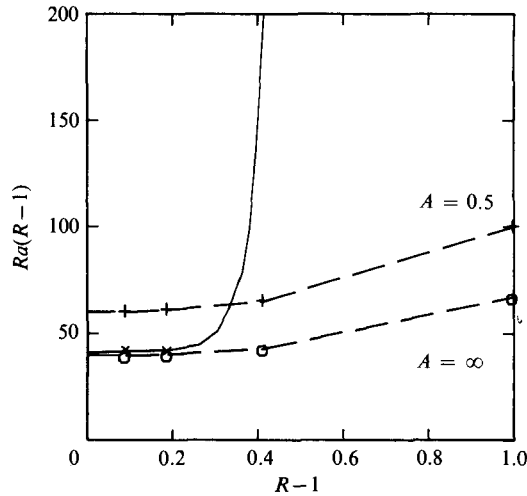
FIGURE 19. A schematic stability curve for type I solutions in a three-dimensional setting. The dashed lines correspond to three-dimensional bifurcations (Caltagirone 1976) while the solid line corresponds to two-dimensional bifurcations (present paper).

supported by experimental observations conducted in horizontal annuli containing Newtonian fluids (see, for example, Liu, Mueller & Landis 1961).

Things are somewhat clearer for the case of aspect ratio $A = 0.5$. Obviously, in that case, when $R < 1.34$, the bifurcation from two-dimensional bicellular to multicellular flow will occur. As the Rayleigh number increases, the multicellular structure eventually undergoes a secondary bifurcation into oscillatory two- or three-dimensional flow.

6. Conclusion

We carried out a systematic study of two-dimensional, multiple solutions of the DOB equations. For low Rayleigh numbers $(Ra < Ra_c)$, the DOB equations possess a unique solution. For $Ra > Ra_c$, multiple solutions exist.

For relatively large radii ratios $R > 2^{\frac{1}{3}}$, the additional solutions appear as isolated branches. Two solutions remain stable for some range of Rayleigh numbers $Ra > Ra_c$ until eventually they lose stability via Hopf bifurcations. Which solution will be observed in an experiment depends on the initial conditions.

For relatively small radii ratios $R < 2^{\frac{1}{3}}$, the additional solutions appear via a simple bifurcation process. One solution branch loses stability while another one gains it. For $Ra > Ra_c$, we find only one stable solution and that loses stability via a Hopf bifurcation as the Rayleigh number is increased.

We observe that at and beyond bifurcation and turning points, the stable branch possesses a higher heat transfer rate, a lower energy content and a higher entropy generation rate than do the unstable branches.

Appendix A

In this Appendix the recurrence relations resulting from the substitution of expression (3.4) into (3.2) are listed.

From the momentum equations (3.2b), we get

$$A_{s,p,l} = \frac{1}{(\pi^2\alpha^2 p^2 + l^2)}\left\{\sum_{m=1}^{\infty} B_{(s-1),m,(l-1)}\left[-\tfrac{1}{2}\pi^2\alpha^3 m\, c(m,p)\right.\right.$$
$$\left.\left. + \tfrac{1}{2}\alpha(l-1)\,D(m,p)\right] + B_{(s-1),m,(l+1)}\,\tfrac{1}{2}\pi^2\alpha^3 m\, C(m,p) + \tfrac{1}{2}\alpha(l+1)\,D(m,p)\right],\right\} \quad \text{(A 1)}$$

where
$$C(m,p) = (p+m)\left(\frac{1-e^{\frac{1}{\alpha}}(-1)^{p+m}}{1+\pi^2\alpha^2(p+m)^2}\right) + (p-m)\left(\frac{1-e^{\frac{1}{\alpha}}(-1)^{(p-m)}}{1+\pi^2\alpha^2(p-m)^2}\right), \quad \text{(A 2)}$$

$$D(m,p) = \left(\frac{e^{\frac{1}{\alpha}}(-1)^{m-p}-1}{1+\pi^2\alpha^2(m-p)^2}\right) - \left(\frac{e^{\frac{1}{\alpha}}(-1)^{(m+p)}-1}{1+\pi^2\alpha^2(m+p)^2}\right). \quad \text{(A 3)}$$

Energy equation (3.2a) gives

$$B_{s,p,l} = \frac{\alpha}{p^2\pi^2\alpha^2+l^2}\left[l A_{s,p,l} - \tfrac{1}{4}\pi\sum_{k=1}^{s-1} Q_{s,k,p,l}\right], \quad \text{(A 4)}$$

where
$$Q_{s,k,p,l} = \epsilon_l\left\{\sum_{i=1}^{p-1}\sum_{j=0}^{l-1}(il-jp)B_{(s-k),i,j}A_{k,(p-i),(l-j)} + \sum_{i=1}^{M-p}\sum_{j=0}^{l-1}(il+jp)B_{(s-k),i,j}A_{k,(p+i),(l-j)}\right.$$

$$+ \sum_{i=1+p}^{M}\sum_{j=0}^{l-1}(jp-il)B_{(s-k),i,j}A_{k,(i-p),(l-j)} + \sum_{i=1}^{p-1}\sum_{j=0}^{N-l}(il+jp)B_{(s-k),i,j}A_{k,(p-i),(l+j)}$$

$$+ \sum_{i=1}^{M-p}\sum_{j=0}^{N-l}(il-jp)B_{(s-k),i,j}A_{k,(p+i),(l+j)} + \sum_{i=1+p}^{M}\sum_{j=0}^{N-l}(-il-jp)B_{(s-k),i,j}A_{k,(i-p),(l+j)}$$

$$+ \sum_{i=1}^{p-1}\sum_{j=1+l}^{N}(jp-il)B_{(s-k),i,j}A_{k,(p-i),(j-l)} + \sum_{i=1}^{M-p}\sum_{j=1+l}^{N}(-il-jp)B_{(s-k),i,j}A_{k,(p+i),(j-l)}$$

$$\left. + \sum_{i=1+p}^{M}\sum_{j=1+l}^{N}(il-jp)B_{(s-k),i,j}A_{k,(i-p),(j-l)}\right\}, \quad \text{(A 5)}$$

$$\epsilon_l\begin{cases} = \tfrac{1}{2} & \text{for } l = 0 \\ = 1 & \text{for } l > 0 \end{cases}$$
$$\alpha = 1/\log R,$$

and $A_{s,p,l} = B_{s,p,l} = 0$, unless $l \leqslant s$ and either both s and l are even or both s and l are odd.

Appendix B

In this Appendix, we investigate the effects of both finite machine precision and truncation of the Fourier expansion (3.4) on the accuracy of the coefficients N_s in table 1.

Most of the computations were carried out on the Univac 1100 with 18-digits precision. In order to test possible adverse effects of round-off errors, we repeated one of the computations ($R = 2^{\frac{1}{4}}$) on the Cray-1 with 27-digits precision. The first 15 digits of the coefficients N_s were reproduced exactly. Thus, we concluded that finite machine precision did not adversely affect our results.

Next, the level of truncation (M, N) in the spectral presentation (3.4) was

(M,N)			
s	28×28	32×32	33×33
10	$-4.0544\ (-74)$	$-4.0550\ (-74)$	$-4.0554\ (-74)$
20	$2.7102\ (-135)$	$2.7102\ (-135)$	$2.7102\ (-135)$
30	$2.0305\ (-190)$	$1.3560\ (-190)$	$1.3560\ (-190)$

TABLE 3

		Consecutive terms (C1)		Alternate terms (C2)	
	Ratio	Linear extrapolation	Quadratic extrapolation	Linear extrapolation	Quadratic extrapolation
s	$(c_s^0)^{-2}$	$(c_s^1)^{-2}$	$(c_s^2)^{-2}$	$(c_s^1)^{-2}$	$(c_s^2)^{-2}$
25	117	119	101	120	121
26	117	121	164	120	121
27	118	119	100	120	121
28	118	122	172	121	122
29	118	120	99	121	122
30	118	122	185	121	122

TABLE 4. Neville table for $R = 2^{\frac{1}{2}}$

examined. This was done by comparing results obtained for the coefficients N_s in (3.6) for various choices of (M,N). Table 3 provides a representative example. The values obtained for a few coefficients N_s are listed for radii ratio $R = 2^{\frac{1}{8}}$. It appears that the results used in this paper are accurate within 4 significant digits.

Appendix C

In this Appendix, the construction of Neville tables is briefly described.

The Neville table to the sequence $\{c_s^0\}$, where $c_s^0 \equiv N_s/N_{s-1}$ is a triangular arrangement of the elements c_s^k, where s labels the rows and $k = 0, 1, 2, ..., s$, the columns. The elements of the kth column are generated from the $(k-1)$th by

$$c_s^k = \frac{sC_s^{k-1} - (s-k)\,C_{s-1}^{k-1}}{k}, \quad k \geqslant 1. \tag{C 1}$$

If the sequence (c_s^0) is considered as a function of $(1/s)$, the element c_s^k is the intercept on the $1/s = 0$ axis of the kth-degree curve through $(k+1)$ successive points $c_{s'}^0, c_{s-1}^0, ..., c_{s-k}^0$.

Unfortunately, the Neville table may tend to magnify any small irregularities in the initial sequence; thus, in some cases (Bowers & Woolf 1969), the following equation, in place of (C 1) may yield better results:

$$c_s = \frac{sc_s^{k-1} - (s-2k)\,c_{s-2}^{k-1}}{2k}. \tag{C 2}$$

Ra_c values predicted by the Neville tables (table 4) utilizing the consecutive terms (C 1) and alternate terms (C 2) are listed in table 4. The Neville table constructed for the consecutive terms (C 1) exhibits somewhat oscillatory behaviour while the one constructed for the alternate terms (C 2) predicts more consistent results.
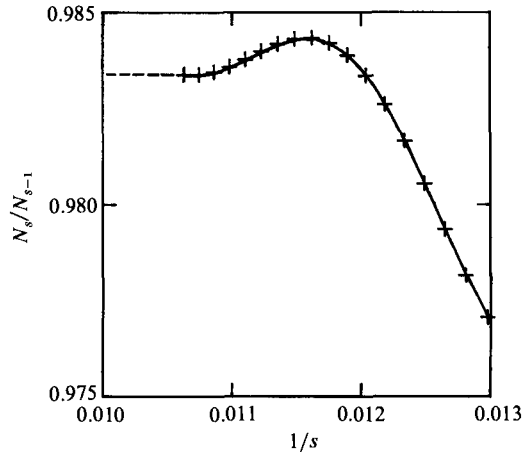
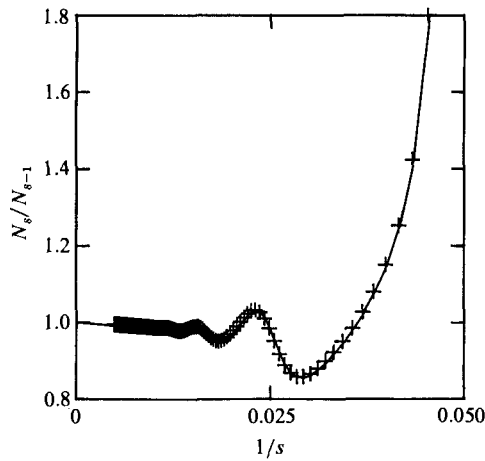FIGURE 20. Domb–Sykes plot of the series (D2) with 94 terms.

FIGURE 21. Domb–Sykes plot of the series (D2) with 200 terms.

Appendix D

In this Appendix, we demonstrate that the Domb–Sykes analysis of the truncated Taylor series may lead to an erroneous estimate of the power of the nearest singularity even though the location of the nearest singularity is estimated fairly accurately.

To this end, we consider a simple model function

$$F(z) = (1-z)^{\frac{1}{2}}(z^2 - 2.10z + 1.21)^{-\frac{1}{4}} \qquad (D\ 1)$$

which we expand into the power series

$$F(z) = \sum_{s=0}^{S} N_s z^s. \qquad (D\ 2)$$

The nearest singularity is located at $z = 1$, and $\nu = -0.5$ (3.9). The Domb–Sykes plot consisting of the first 94 terms is depicted in figure 20. The plot appears to exhibit a linear relationship in the ratio N_s/N_{s-1}. Extrapolation of the data leads to an

estimate of the nearest singularity correct to within 2%. The tangent to the curve becomes almost horizontal suggesting that the nearest singularity might be a simple pole ($\nu = 1$) which, of course, is wrong.

In this particular case, we have the luxury of being able to compute as many terms in the expansion as we wish. In figure 21, we show the Domb–Sykes plot which corresponds to 200 terms in the series. This curve predicts correctly both the location of the nearest singularity and its exponent.

Thus, we demonstrate that in situations in which the function $F(z)$ possesses many singularities, the rate of convergence of the Domb–Sykes plot is adversely affected. Should the number of terms available in the corresponding truncated Taylor series, be insufficient, erroneous predictions of the exponent of the nearest singularity may result.

Appendix E

In this Appendix, the nonlinear, algebraic equations which are obtained from the nonlinear p.d.e.'s (2.2) via projection are listed.

From the momentum equation (2.2*a*), we have

$$
\begin{aligned}
A_{p,l} = \frac{2\alpha Ra}{p^2\pi^2\alpha^2 + l^2} \epsilon_l \bigg\{ & \frac{p\pi\alpha^2[1 - (-1)^p \, e^{1/\alpha}]}{(p^2\pi^2\alpha^2 + l^2)} \\
& + \sum_{i=1}^{M-l} \tfrac{1}{2} i\pi\alpha \, C(i,p) \left[-B_{i,(l-1)} + B_{i,(l+1)} \right] \\
& + \sum_{i=1}^{M-l} \tfrac{1}{2} D(i,p) \left[(l-1) B_{i,(l-1)} + (l+1) B_{i,(l+1)} \right] \bigg\}
\end{aligned}
\tag{E 1}
$$

where
$$
\epsilon_l = \begin{cases} 1 & \text{for } l = 1, \\ 0 & \text{for } l > 1. \end{cases}
$$

Here the functions $C(i,p)$ and $D(i,p)$ are the same as those defined by (A 2) and (A 3) given in Appendix A.

Energy equation (2.2*a*) is used to define the residue $F_{p,l}$ as

$$
F_{p,l} = B_{p,l} - \frac{\alpha l A_{p,l} - (\pi\alpha)\tfrac{1}{4} Q^*_{p,l}}{(p^2\pi^2\alpha^2 + l^2)},
\tag{E 2}
$$

where $Q^*_{p,l}$ is identical with $Q_{s,k,p,l}$ as given by (A 5) in Appendix A except that the subscripts $(s-k)$ and k are to be dropped in the terms $B_{(s-k),i,j}$ and $A_{k,i,j}$, respectively.

The shape matrix introduced in (4.2) is given by

$$
S_{m,p,l} = \frac{\alpha}{2(p^2\pi^2\alpha^2 + l^2)} \left\{ \frac{e^{\frac{2}{\alpha}}(-1)^{m+p} - 1}{1 + \tfrac{1}{4}(m+p)^2\pi^2\alpha^2} - \frac{e^{\frac{2}{\alpha}}(-1)^{m-p} - 1}{1 + \tfrac{1}{4}(m-p)^2\pi^2\alpha^2} \right\}
\tag{E 3}
$$

REFERENCES

AIDUN, C. K. & STEEN, P. H. 1987 Transition to oscillatory convective heat transfer in a fluid-saturated porous medium. *J. Thermophys. Heat Transfer* **1**, 268–273.

BAKER, G. A. 1965 The theory and application of the Padé approximant method. in *Advances in Theoretical Physics* (ed. K. A. Brueckner), vol. 1, pp. 1–58. Academic.

BAKER, G. A. & GAMMEL, J. L. (eds) 1970 *The Padé Approximant in Theoretical Physics.* Academic.

BAU, H. H. 1984 Thermal convection in a horizontal, eccentric annulus containing a saturated porous medium – an extended perturbation expansion. *Intl J. Heat Mass Transfer* **27**, 2277–2787.

BEJAN, A. 1984 *Convection Heat Transfer*, p. 355. Wiley.

BOWERS, R. G. & WOOLF, M. E. 1969 Some critical properties of the Heisenberg model. *Phys. Rev.* **177**, 917–932.

BRAILOVSKAYA, V. A., PETRAZHITSKII, G. B. & POLEZHAEV, V. I. 1978 Natural convection and heat transfer in porous interlayers between horizontal coaxial cylinders. *J. Appl. Mech. Tech. Phys.* **19**, 781–785.

BURNS, P. J. & TIEN, C. L. 1979 Natural convection in porous media bounded by concentric spheres and horizontal cylinders. *Intl J. Heat Mass Transfer* **22**, 929–939.

CALTAGIRONE, J. P. 1976 Thermoconvective instabilities in a porous medium bounded by two concentric horizontal cylinders. *J. Fluid Mech.* **76**, 337–362.

DECKER, D. W. & KELLER, H. B. 1980 Solution branching – a constructive technique. In *New Approaches to Nonlinear Problems in Dynamics* (ed. P. J. Holmes), pp. 53–69. Philadelphia: SIAM.

DOMB, C. & SYKES, M. F. 1957 On the susceptibility of a ferromagnetic above the Curie point. *Proc. R. Soc. Lond.* **A240**, 214–228.

FULKS, W. 1961 *Advanced Calculus.* Wiley.

GAUNT, D. S. & GUTTMANN, A. J. 1974 Asymptotic analysis of coefficients. In *Phase Transition and Critical Phenomena* (ed. C. Domb & M. S. Green), pp. 181–243. Academic.

HENRICI, P. 1977 *Applied and Computational Complex Analysis.* Wiley.

HIMASEKHAR, K. 1987 Thermal convection in a horizontal eccentric annulus filled with a saturated porous medium. Ph.D. dissertation. University of Pennsylvania, Philadelphia.

HUNTER, C. & GUERRIER, B. 1980 Deducing the properties of singularities of functions from their Taylor series coefficients. *SIAM J. Appl. Maths* **39**, 248–263.

LANG, S. 1985 *Complex Analysis.* Springer.

LAPWOOD, E. R. 1948 Convection of a fluid in a porous medium. *Proc. Camb. Phil. Soc.* **44**, 508–521.

LIU, C. Y., MUELLER, W. K. & LANDIS, F. 1961 Natural convection heat transfer in long horizontal cylindrical annuli. *International Developments in Heat Transfer*, vol. V, pp. 976–984. ASME.

RAO, Y. F., FUKUDA, K. & HASEGAWA, S. 1986 Steady and transient analyses of natural convection in a horizontal porous annulus with Galerkin method. *Proc. AIAA/ASME 4th Thermophysics and Heat Transfer Conference, HTD-Vol. 56* (ed. V. Prasad & N. A. Hussain), pp. 95–104. Boston, MA.

VAN DYKE, M. 1974 Analysis and improvement of perturbation series. *Q.J. Mech. Appl. Maths* **27**, 423–450.

VAN DYKE, M. 1975 Computer extension of perturbation series in fluid mechanics. *SIAM J. Appl. Maths* **28**, 720–734.